



**UNIVERSIDAD DE INVESTIGACIÓN DE
TECNOLOGÍA EXPERIMENTAL YACHAY**

Escuela de Ciencias Físicas y Nanotecnología

**TÍTULO: MEASURING THE SPIN-POLARIZATION OF
OLIGOPEPTIDE MOLECULE: AB INITIO AND TIGHT-
BINDING CALCULATION**

Trabajo de integración curricular presentado como requisito para
la obtención del título de Físico.

Autor:

Raúl Alejandro Hidalgo Sacoto

Tutor:

Ph.D Duncan J.Mowbray

Co-tutor:

Ph.D Ernesto Medina

Urcuquí, Mayo 2021

SECRETARÍA GENERAL
(Vicerrectorado Académico/Cancillería)
ESCUELA DE CIENCIAS FÍSICAS Y NANOTECNOLOGÍA
CARRERA DE FÍSICA
ACTA DE DEFENSA No. UITEY-PHY-2021-00007-AD

A los 2 días del mes de junio de 2021, a las 12:00 horas, de manera virtual mediante videoconferencia, y ante el Tribunal Calificador, integrado por los docentes:

Presidente Tribunal de Defensa	Dra. PERALTA ARCIA, MAYRA ALEJANDRA DE JESUS , Ph.D.
Miembro No Tutor	Dr. COSENZA MICELI, MARIO GIUSEPPE , Ph.D.
Tutor	Dr. MOWBRAY , DUNCAN JOHN , Ph.D.

El(la) señor(ita) estudiante HIDALGO SACOTO, RAUL ALEJANDRO, con cédula de identidad No. 1314467612, de la ESCUELA DE CIENCIAS FÍSICAS Y NANOTECNOLOGÍA, de la Carrera de FÍSICA, aprobada por el Consejo de Educación Superior (CES), mediante Resolución RPC-SO-39-No.456-2014, realiza a través de videoconferencia, la sustentación de su trabajo de titulación denominado: **MEASURING THE SPIN-POLARIZATION OF OLIGOPEPTIDE MOLECULE: AB INITIO AND TIGHT BINDING CALCULATION**, previa a la obtención del título de FÍSICO/A.

El citado trabajo de titulación, fue debidamente aprobado por el(los) docente(s):

Tutor	Dr. MOWBRAY , DUNCAN JOHN , Ph.D.
Co - Tutor	Dr. MEDINA DAGGER, ERNESTO ANTONIO , Ph.D.

Y recibió las observaciones de los otros miembros del Tribunal Calificador, las mismas que han sido incorporadas por el(la) estudiante.

Previamente cumplidos los requisitos legales y reglamentarios, el trabajo de titulación fue sustentado por el(la) estudiante y examinado por los miembros del Tribunal Calificador. Escuchada la sustentación del trabajo de titulación a través de videoconferencia, que integró la exposición de el(la) estudiante sobre el contenido de la misma y las preguntas formuladas por los miembros del Tribunal, se califica la sustentación del trabajo de titulación con las siguientes calificaciones:

Tipo	Docente	Calificación
Miembro Tribunal De Defensa	Dr. COSENZA MICELI, MARIO GIUSEPPE , Ph.D.	10,0
Presidente Tribunal De Defensa	Dra. PERALTA ARCIA, MAYRA ALEJANDRA DE JESUS , Ph.D.	10,0
Tutor	Dr. MOWBRAY , DUNCAN JOHN , Ph.D.	10,0

Lo que da un promedio de: **10 (Diez punto Cero)**, sobre 10 (diez), equivalente a: **APROBADO**

Para constancia de lo actuado, firman los miembros del Tribunal Calificador, el/la estudiante y el/la secretario ad-hoc.

Certifico que en cumplimiento del Decreto Ejecutivo 1017 de 16 de marzo de 2020, la defensa de trabajo de titulación (o examen de grado modalidad teórico práctica) se realizó vía virtual, por lo que las firmas de los miembros del Tribunal de Defensa de Grado, constan en forma digital.

HIDALGO SACOTO, RAUL ALEJANDRO
 Estudiante



Dra. PERALTA ARCIA, MAYRA ALEJANDRA DE JESUS , Ph.D.
 Presidente Tribunal de Defensa

Digitally signed by
 MAYRA ALEJANDRA DE JESUS PERALTA ARCIA
 Date: 2021.06.02 13:13:25 -05'00'

Dr. MOWBRAY , DUNCAN JOHN , Ph.D.
Tutor



Firmado electrónicamente por:
**DUNCAN JOHN
MOWBRAY .**

Dr. COSENZA MICELI, MARIO GIUSEPPE , Ph.D.
Miembro No Tutor



Firmado electrónicamente por:
**MARIO GIUSEPPE
COSENZA MICELI**

CIFUENTES TAFUR, EVELYN CAROLINA
Secretario Ad-hoc

EVELYN
CAROLINA
CIFUENTES TAFUR

Digitally signed by
EVELYN CAROLINA
CIFUENTES TAFUR
Date: 2021.06.02
13:07:23 -05'00'

AUTORIA

Yo, RAUL ALEJANDRO HIDALGO SACOTO, con cédula de identidad 1314467612, declaro que las ideas, juicios, valoraciones, interpretaciones, consultas bibliográficas, definiciones y conceptualizaciones expuestas en el presente trabajo; así cómo, los procedimientos y herramientas utilizadas en la investigación, son de absoluta responsabilidad de el/la autora (a) del trabajo de integración curricular. Así mismo, me acojo a los reglamentos internos de la Universidad de Investigación de Tecnología Experimental Yachay.

Urcuquí, Mayo y 2021.



Raúl Alejandro Hidalgo Sacoto
CI: 1314467612

AUTORIZACIÓN DE PUBLICACIÓN

Yo, RAUL ALEJANDRO HIDALGO SACOTO, con cédula de identidad 1314467612, cedo a la Universidad de Tecnología Experimental Yachay, los derechos de publicación de la presente obra, sin que deba haber un reconocimiento económico por este concepto. Declaro además que el texto del presente trabajo de titulación no podrá ser cedido a ninguna empresa editorial para su publicación u otros fines, sin contar previamente con la autorización escrita de la Universidad. Asimismo, autorizo a la Universidad que realice la digitalización y publicación de este trabajo de integración curricular en el repositorio virtual, de conformidad a lo dispuesto en el Art. 144 de la Ley Orgánica de Educación Superior. Urcuquí, Mayo 2021.



Raúl Alejandro Hidalgo Sacoto
CI: 1314467612

Dedicatoria

A mis padres Raúl y Yohana, mis hermanos y hermanas, y mis amigos de la U y de Portoviejo.

Acknowledgements

First, of all, I want to thank my parents Yohana and Raúl for the support and guidance during all my life until now, as well as my sisters Ariana, Roberta, Isabela, my stepmother Myriam, step-brother Salomon, and family members I have the opportunity to meet, for their invaluable company and support.

I acknowledge advisor Duncan Mowbray Ph.D. and co-advisor Ernesto Medina Ph.D. for their guidance, useful discussion, and friendship during the bachelor program at Yachay. I want to acknowledge especially Duncan because he introduced me to research for the first time in 3rd year, and since then I have found my way into physics.

To my latest tutors, Jiri Svozilik Ph.D. and Francisco Muñoz Ph.D., thank you for the trust and guidance during the research period we share and show me the way to the quantum world. Especially, I want to acknowledge my colleagues at the Theoretical Chemical Physics Group at Chile University and hope soon be able to see them again.

To my friends, with whom I spent hours and hours full of emotions and random situations, I want to say thanks for being my second family. To Mayra, Evelin and Nicole, thank you for sharing the department and for putting up with me, as well as all the adventures we had with and without Eve's car; Sabrina, Daniela y Genesis, thank you for the parties and the late-night meetings, and of course the camping we never did; Stefano, Gino, and Isabel, thank you for the fidelity and, as well as the lunch and bielitas we share together, you always manage to make me feel at home; Carito, Mateo and Samantha, thank you for all the lovely meals and drinks we share together, and of course the basketball games we enjoy; and Jennifer, thank you for being the best partner in the nice and difficult times.

To all of you, I have my sincerest gratitude.

I appreciate truly the education given by Yachay Tech and the School of Physical Sciences and Nanotechnology, as well as the resources and opportunities provided, from the courses to the clubs. Special acknowledgment to our former secretary Evelyn, and Graciela Ph.D., for their formidable support during my studies.

This work employed the Imbabura cluster of Yachay Tech University, which was purchased under contract No. 2017-024 (SIE-UIITEY-007-2017).

Resumen

Los experimentos recientes han mostrado un interés significativo en moléculas biológicas como ADN, proteínas, oligopéptidos y aminoácidos. Tales moléculas tienen en común su estructura quiral, la simetría de reversión al tiempo y la ausencia de interacciones de intercambio magnético. La actividad de filtrado de espín se debe a la interacción intrínseca espín-órbita o espín-órbita acoplada a la presencia de fuentes locales fuertes de campos eléctricos. Aquí, derivamos un modelo analítico usando un hamiltoniano de amarre-fuerte para oligopéptidos que incluye tantas interacciones de Rashba inducidas por la unión de hidrógeno e interacciones intrínsecas. Utilizamos un esquema plegable de la teoría de la teoría de la perturbación de primer orden y derivamos el Hamiltoniano en espacio recíproco con términos intrínsecos y Rashbas para evaluar la actividad de filtrado del oligopéptido. Cálculos de primeros principios usando Teoría de Función de Densidad se realizan para estudiar la estructura electrónica de la molécula quiral y su relación con el efecto del filtrado de giros. El transporte electrónico se mide utilizando el método de funciones de Green fuera de equilibrio para estudiar la actividad de filtrado de espín en una superficie de oro. El acuerdo cualitativo que obtenemos con experimentos recientes muestra el importante papel desempeñado por la unión de hidrógeno en la actividad de giro, pero falta una descripción adecuada en el contexto de primeros principios.

Palabras claves: espintrónica, quiralidad, oligopéptido, espín-órbita, teoría de función de densidad, amarre fuerte, transporte electrónico.

Abstract

Recent experiments have shown significant spin activity in biological molecules such as deoxyribonucleic acid (DNA), proteins, oligopeptides, and aminoacids. Such molecules have in common their chiral structure, time-reversal symmetry and the absence of magnetic exchange interactions. The spin activity is then assumed to be due to either the intrinsic spin orbit (SO) interaction or SO coupled to the presence of strong local sources of electric fields. Herein, we derive an analytical tight binding (TB) Hamiltonian model for oligopeptides that includes both intrinsic SO and Rashba interactions induced by hydrogen bonding. We use a lowest order perturbation theory band-folding scheme and derive the reciprocal space intrinsic and Rashba type Hamiltonian terms to evaluate the spin activity of the oligopeptide. *Ab initio* calculations are performed to study the electronic structure of the chiral molecule and its relation to the spin filtering effect. Electronic transport is measured using the non-equilibrium Green's function (NEGF) method for studying the spin activity in a Au surface. The qualitative agreement we obtain with recent experiments shows the important role played by hydrogen bonding in spin activity, but proper description in *ab initio* context is lacking.

Keywords: spintronics, chirality, oligopeptide, spin-orbit coupling (SOC), density functional theory (DFT), tight binding (TB), electronic transport (ET)

Contents

List of Figures	xii
List of Tables	xiii
1 Introduction	1
1.1 General and Specific Objectives	3
1.2 Overview	3
2 Theoretical Background	5
2.1 Density functional theory	5
2.1.1 The Schrödinger equation	5
2.1.2 Born–Oppenheimer approximation	6
2.1.3 Periodic systems	6
2.1.4 Reciprocal space	7
2.1.5 The Hohenberg–Kohn theorem	8
2.1.6 Self-consistent Kohn–Sham system	9
2.1.7 Spin-polarized density functional theory	11
2.1.8 XC functionals	12
2.2 Representations of the Kohn–Sham wavefunctions	14
2.2.1 Plane wave	15
2.2.2 Linear combination of atomic orbitals	16
2.2.3 Basis sets generation for linear combination of atomic orbitals	16
2.2.4 Projector augmented wave method	17
2.3 Analytical Tight binding models	18
2.3.1 Slater–Koster components	19
2.3.2 Intrinsic spin-orbit coupling	20
2.3.3 Derivation of the band folding method	20
2.4 Non-equilibrium Green’s function calculations using density functional theory	21

2.4.1	Non-equilibrium electronic transport in a contact-electrode system	22
2.4.2	Non-equilibrium Green's function implementation	23
2.5	Oligopeptide	24
3	Methodology	27
3.1	Tight binding model for a chiral molecule	27
3.2	Spin-polarized calculations with linear combination of atomic orbitals basis sets	29
3.3	Electronic transport calculations in the atomic simulation environment	29
4	Results & Discussion	31
4.1	Derivation of effective Hamiltonian	31
4.1.1	The effective model	31
4.1.2	Bloch Space effective Hamiltonian	33
4.1.3	Hamiltonian in vicinity of half filling	34
4.2	Electronic transport through α helix alanine oligopeptide	36
4.2.1	Length dependence of α helix alanine oligopeptide's wavefunctions	36
4.2.2	Electronic transport through a α helix alanine oligopeptide (α -HAO)@Au slabs(111) junction	38
5	Conclusions and Outlook	41
A	Parameters for the effective Hamiltonian	43
B	Full Hamiltonian	45
C	Slater-Koster integrals	47
D	Full linear combination of atomic orbitals Hamiltonian construction: overlaps and couplings	49
	Bibliography	51
	Abbreviations	61

List of Figures

2.1	Kohn–Sham (KS) self-consistent scheme	10
2.2	Slater–Koster (SK) sides A and B. The SK kinetic overlaps is defined by the three angles $\mathbf{l} = \cos(\alpha)$, $\mathbf{m} = \cos(\beta)$ and $\mathbf{n} = \cos(\gamma)$, defined by the cosine of the angle from the principal axis to the vector joining side A and B.	19
2.3	The scattering region or junction is composed of left (L) and right (R) electrode leads and a central (C) region, with Hamiltonians h_1 , h_2 , and h , respectively. Each junction includes at least two principal layer (PL) which only couple between neighbors. In our density functional theory (DFT) calculations we included only one PL in the left lead, manually adding a second PL to h_1 as described in Appendix D.1. The central region includes the molecule with linker group at its ends ensuring its stability on the electrodes.	24
2.4	Structural schematics of (a) alanine (ala) and (b) right-handed α -HAO in vacuum. C, N, O, and H atoms are depicted as grey, blue, red, and white balls, respectively.	25
3.1	Schematic representation of the scattering region with gold (Au)(111) six layer 5×6 surface slabs as electrodes of 180 atoms on side and the two turn α -HAO chiral molecule and amino ($-\text{NH}_2$) linker groups with chemical formula $\text{C}_{24}\text{N}_9\text{O}_8\text{H}_{43}$ forming the junction. C, N, O and H atoms are shown in grey, blue, red, and white, respectively.	29
4.1	(a) Front view of the helical oligopeptide in the xy -plane. Here h is the helical pitch and each p -orbital are labelled. The internal electric field caused by the hydrogen bond high polarization and the component along each direction are shown in red. (b) Top view of the helical oligopeptide in the XZ -plane where r represents the radius of the helix, and $\Delta\varphi$ is the angle between consecutive amino acids (AAs). Extracted from Torres <i>et al.</i> ¹	32
4.2	Kinetic spin degenerate bands with K_{\pm} points(black) and a doped point (orange) taken at $k_F = 3\pi/5$. The values for the parameters are described in Tables A.1A.2.	35
4.3	Spatial distribution of KS wavefunctions for two turns α -HAO (a) highest occupied molecular orbital (HOMO) and (b) lowest unoccupied molecular orbital (LUMO), and three turns α -HAO (c) HOMO and (d) LUMO. Positive and negative phases of the wavefunctions are in red and blue. C, N, O, and H atoms are shown in grey, blue, red, and white, respectively.	36

4.4	Density of states (DOS) of α -HAO in gas phase with two (red) and three (purple) turns as a function of energy ε in eV relative to the Fermi level ε_F	37
4.5	(a) HOMO and (b) LUMO pinned to the Fermi level ε_F of the α -HAO@Au(111) junction. Positive and negative isosurfaces are shown in red and blue, respectively. (c) projected density of states (PDOS) in eV^{-1} localized on the α -HAO molecule (black) and Au(111) surface (yellow) and (d) transmission $T(\varepsilon)$ through spin up and spin down channels through the α -HAO@Au(111) junction versus energy ε relative to the Fermi level, ε_F , in eV. The eigenenergies of (i), (ii), (iii), (iv), (v), (vi) levels shown in Fig. 4.6 are marked in (c).	39
4.6	Spatial distribution of the KS wavefunctions for the α -HAO@Au(111) junction marked in Fig. 4.5(c), and their eigenenergies in eV relative to the Fermi level ε_F . Positive and negative isosurfaces are shown in red and blue, respectively.	40
D.1	To the left: Matrix distribution of linear combination of atomic orbitals (LCAO) components of the setup used in this study. To the right: Re-arrangement of the LCAO overlap matrices, by adding one PL to the left of the scattering region. Notice that the dimension of the LCAO Hamiltonian increase from 3178×3178 to 3988×3988 , that includes LCAO site energies and overlap terms from the added PL, to the rest of the scattering region. The purple square in the upper left corner represent the same overlap matrices between PLs as the one present in the lower right matrix elements of PLs.	50

List of Tables

3.1	SO matrix elements between p orbitals in the local coordinate system.	27
3.2	LCAO basis set and number of basis functions employed for each atomic species.	30
A.1	Left column: SK parameters for s and p orbitals from ² . Center column: Atomic parameters for carbon atoms from ^{2,3} Right column: Structural parameters used to describe the oligopeptide ⁴ . In realistic systems, $\Delta\phi$ is different than $\pi/2$, but this value is used to have a commensurable system. . .	43
A.2	Estimation of effective interactions for the system. Left column: Hopping interactions. Right column: SO interactions.	43
B.1	The matrix elements of the full Hamiltonian in the local coordinate system corresponding to Eq 3.10. The π and σ spaces are the diagonal components while the off-diagonal correspond to T and T^\dagger of (3.10).	45

Chapter 1

Introduction

In Ecuador, technologies are mostly imported and then assembled locally, leaving no actual economic interest in the fabrication of novel devices for technological development. The demand for technologies is covered mainly by foreign industries and by the development in technology transfer centers. However, the production of highly specialized devices is missing from Ecuadorian industry⁵. This demonstrates both the need for research and applicable innovation within these areas, and the development of materials for the fabrication of electronic devices.

High-density devices, with high speeds and low energy consumption, are in high demand for the implementation of several new technologies. In order to achieve considerable improvement in actual current power, a universal memory with these characteristics is required. Possible solutions will implement random access memory (RAM), devices that can manage and store dynamically working data and machine code. Two potential solutions are magnetic memories⁶ and spin-transfer torque memory⁷. Both technologies offer high density storage while using a permanent magnet on a small scale at room temperature. However, such a small-scale fabrication can be problematic for their production.

According to Moore's law⁸, the density of transistors on a chip should double every two years, as a rule of thumb. In the industry, this principle has been historically followed by the technological development of computational power for individual chips. However, as the size of the processor continues to shrink, electrons tend to move faster, producing a heat source. This effect has jammed the circuitry in smaller areas, losing the law's exponential growth.⁹ Enormous research efforts are now being made worldwide in order to continue following Moore's Law, but with fundamentally different methods, even going outside of classical physics's established technologies, such as quantum computing. As processes are computed in physically smaller devices, quantum mechanical effect come into play and may even be controlled at the atomic level. Quantum computing, which promises sub-exponential time for certain types of calculations, is advancing to achieve quantum supremacy over classical computing by taking advantage of quantum effects.

Several solutions have been raised during the years for achieving greater computational power by crafting more powerful devices or processors. One candidate is 2D-graphene-like compounds, such as transition-metal dichalcogenides. These atomically thin compounds are capable of being the building blocks of next-generation

atomic circuits¹⁰. Another promising candidate is spintronics, which allows computing by flipping electron spins rather than by moving electrons, thus avoiding heat production¹¹. This opens the possibility of developing nanoscale devices for information storage and magnetic sensing with improved performance by considering the spin as the fundamental piece of information for computation.

In 1988, a giant magnetoresistance was found in a trilayer heterostructure composed of a thin non-magnetic layer “sandwiched” between two ferromagnetic electrode. This was the first experimental realization of a spin valve¹². Since then, a range of applications of spintronics have arisen, from read-head devices, to non-volatile magnetic memories (MRAM), to spin states as quantum bit, to nano-oscillators for applications in wireless networks¹³. As the field has evolved, there has been a transition from the usage of inorganic metals and semiconductor-based spin valves, to molecular-organic-based ones.

Organic molecules offer convenient electronic characteristic, such as weak spin scattering mechanics and long spin life time, on the order of seconds. This makes them ideal for storing and manipulating spin degrees of freedom¹⁴. Other perks compared to inorganic conductors and semiconductors are their capability to be modified, processability, considerably low density, and high flexibility¹⁵.

Chirality refers to a fundamental symmetry property of particles, molecules, and structures such as hands. This is more formally described as the lack of parity symmetry. This kind of enantiomeric class of molecules shows fascinating behavior when they react with other chiral molecules, resulting in different interactions for different combinations. In spintronics, chirality plays an interesting role in determining the magnetic states within the molecule. Since the spin can be used as an additional degree of freedom for electronic processes, the interactions between chirality and spin contribute via an enantiomeric dependence of the electrical resistance in chiral conductors¹⁶.

The electron’s magnetic moment or spin is a quantum property induced by a magnetic field. The Pauli exclusion principle establishes that paired electrons should have opposite spins, enabling the formation of atomic states and chemical bond formation. Controlling spin states or orientation has proved to be a challenge. Typically, spin states can be manipulated only by external magnetic fields or by proximity to ferromagnetic or paramagnetic materials.

In 1999, Ray *et al.*¹⁷ discovered spin filtering in organic chiral molecules without the use of a conventional permanent magnet. This effect is the so-called chiral-induced spin selectivity (CISS). Despite weak spin-orbit coupling (SOC) and nonmagnetic properties, organic chiral molecules exhibit strong spin selectivity at room temperature. Göhler *et al.*¹⁸ first reported the CISS effect in self-assembled monolayers of double-strand deoxyribonucleic acid (dsDNA) adsorbed on Au surfaces, and its length dependence. Later, Mishra *et al.*¹⁹ reported spin-dependent photoelectron transmission and electrochemical behavior on a purple membrane containing bacteriorhodopsin deposited on gold. Further experiments shows spin-dependent electronic transport (ET) in single helical molecules²⁰. This behaviour seems to be typical for chiral organic molecules, and allows the manipulation of spin rather than charge without a permanent magnet facilitating its production and minimization. Chiral molecules have received enormous attention because of interesting features involving their ET and tunneling as a non-equilibrium process. It has been proposed that in equilibrium, chiral molecules like deoxyribonucleic acid (DNA) or oligopeptides exhibit zero spin-polarization in the ground state because of an enantiospecific interaction with a non-chiral surface²¹

Atomic spin orbit (SO) interaction, even of small magnitudes, can be produced by inelastic effects, resulting in high polarization^{20,22–24}. The qualitative explanation for spin activity, in the absence of time-reversal symmetry

breaking interactions, may be studied from one of three theoretical perspectives. Firstly, by using tight binding (TB) models to describe ET due to helical molecules such as oligopeptides and DNA^{25–27}, secondly, by employing spin dependent scattering theory²³ and thirdly, by applying models that include significant SOC terms from the metal substrate as spin filtering sources by angular momentum selections²⁸. Although the atomic SO coupling of carbon-based molecules is quite low (~ 3.5 meV), recent work has shown that helical organic molecules exhibit high electronic polarization and spin filtering capabilities^{1,29–31}.

Recently, important attention has been paid to electron spin polarizing properties of biological chiral molecules such as amino acids (AAs), oligopeptides, proteins, and DNA^{32 18 33 34}. The CISS effect as a spin activity can be explained by two main interactions: time-reversal symmetry breaking³⁵, and the atomic spin-orbit interaction^{22 23}.

Experimentally, several techniques have been used to study the spin filtering of chiral molecules. Of these, conductive probe atomic force microscopy (CP-AFM) is an effective tool to measure and characterize electrical spin activity on the nanometer scale. Other methods, including magnetic conductive atomic force microscopy (mc-AFM)³², spin-dependent electrochemistry (SDE),³⁶ and spin-dependent charge polarization (SDCP)³⁷, may be used to measured spin-dependent conduction and spin-dependent charge polarization. Spintronics in chiral molecules provides a powerful source of spin polarization for high-density materials. Novel applications involving chiral molecules include light-induced magnetic devices³⁸ and molecular semiconductor interfaces to control and detect spin activity for quantum information applications³⁹.

1.1 General and Specific Objectives

The general goal of this thesis is to provide a qualitative explanation of the CISS effect in oligopeptides through *ab initio* and semi-empirical theoretical methods. Direct correlation between *ab initio* calculations and TB models is somewhat lacking in the literature, due to inaccurate representations of the interactions in the TB model and at an *ab initio* level. Specifically, we will employ *ab initio* density functional theory (DFT) and a simple semi-empirical TB model to provide a comparative view, in order to give a better understanding of the properties of polarization through the SO interaction between atoms. As a specific goal of this work, we want to address the length-dependence of the spin dynamics by exploring the wavefunctions involved.

1.2 Overview

This thesis is divided into five chapters and five appendices. We begin by providing in Chapter 2 a theoretical background to DFT, the Kohn–Sham (KS) formalism, exchange and correlation (xc) functional and a description of the approximations most often used. Besides, linear combination of atomic orbitals (LCAO) and projector augmented wave (PAW) are described for further understanding of theory and methods implemented in grid-based projector augmented wave method code (GPAW), the main package used in this thesis for *ab initio* calculations. Additionally, interaction theory-based in tightly bound orbitals is presented for calculating an effective Hamiltonian for any periodic system. Transport calculation is also explained in the context of DFT using propagators. Finally in this chapter, a description of oligopeptides and the physical properties of their geometry is given.

In the third chapter titled Methodology, TB model for a chiral molecule, Spin-DFT calculations for oligopeptide, non-equilibrium Green's function (NEGF)-DFT method for ET are described in detail for further use in the Result & Discussion section.

The fourth chapter, Results & Discussion has two separate parts: we present and discuss TB effective Hamiltonian for a infinite oligopeptide, its Bloch Space representation and in vicinity of electronic half filling dynamics. The second section covers the ground state of the oligopeptide in gas phase, the electronic properties of the α helix alanine oligopeptide (α -HAO)@Au(111), and the spin resolved ET at room temperature.

Finally, in the fifth chapter, Conclusions, we state the length dependent metallic properties of oligopeptides, and further consideration for the observation of CISS effect in the *ab initio* context. Also, we state the importance of SO effects in the chiral molecule for CISS. We discuss future work covering structural and chemical considerations for our model.

In the appendices, we present the SK parameters and the Full Hamiltonian used in the effective Hamiltonian, as well as the LCAO Hamiltonian manipulation for ET.

Chapter 2

Theoretical Background

2.1 Density functional theory

2.1.1 The Schrödinger equation

According to Quantum Mechanics, any property related to the electronic structure of atoms or molecules may be described by system's wave function Ψ . Both the system's wave function Ψ and total energy E may be obtained by solving the time-independent Schrödinger equation, $\hat{H}\Psi = E\Psi$. This depends on the position and spin of the system's N_e electrons and N_n nuclei, so that

$$\Psi = \Psi(\mathbf{r}_1, s_1; \mathbf{r}_2, s_2; \dots; \mathbf{r}_{N_e}, s_{N_e}; \mathbf{R}_1, S_1; \mathbf{R}_2, S_2; \dots; \mathbf{R}_{N_n}, S_{N_n}), \quad (2.1)$$

where \mathbf{r}_i and s_i are the position and spin of the i th electron, respectively, and \mathbf{R}_I and S_I are the position and spin of the I th nuclei. The corresponding many-body Hamiltonian \hat{H} may be decomposed in the form

$$\hat{H} = \hat{T}_e + \hat{V}_{ee} + \hat{V}_{en} + \hat{T} + \hat{V}_{nn}, \quad (2.2)$$

where these terms correspond to the kinetic energy of the electrons, the repulsive electron–electron interaction, the attractive electron–nuclei interaction, the kinetic energy of the nuclei, and the repulsive nuclei–nuclei interaction, respectively. This Hamiltonian operator may then be expressed in terms of \mathbf{r}_i , s_i , \mathbf{R}_I , and S_I as

$$\hat{H} = - \sum_{i=1}^{N_e} \frac{1}{2} \nabla_{\mathbf{r}_i}^2 + \sum_{i=1}^{N_e} \sum_{j=i+1}^{N_e} \frac{1}{|\mathbf{r}_i - \mathbf{r}_j|} - \sum_{i=1}^{N_e} \sum_{I=1}^{N_n} \frac{Z_I}{|\mathbf{r}_i - \mathbf{R}_I|} - \sum_{I=1}^{N_n} \frac{1}{2M_I} \nabla_{\mathbf{R}_I}^2 + \sum_{I=1}^{N_n} \sum_{J=I+1}^{N_n} \frac{Z_I Z_J}{|\mathbf{R}_I - \mathbf{R}_J|}, \quad (2.3)$$

where M_I , and Z_I are the atomic mass and number of the I th nuclei, respectively. Herein we have employed atomic units, equating the electron mass, proton charge, Planck's reduced constant, and Bohr's radius to one ($m_e = e = \hbar = a_0 = 1$). Note that (2.3) may be defined under an appropriate boundary condition for a regular infinite solid, then solving $\hat{H}\Psi = E\Psi$, where E is the total energy of the system. In the following section we will show that the final three terms of (2.2) and (2.3) may be incorporated into an external potential, yielding a purely electronic Hamiltonian \hat{H}_e .

2.1.2 Born–Oppenheimer approximation

It is well known that protons and neutrons, as individual particles, have approximately 1800 times the mass of an electron. In terms of kinetic energies, electrons have a much more rapid response to changes in their surroundings with respect to the nuclei. This key observation means that the physical system may be described by fixing the positions of the atomic nuclei and solving a purely electronic Hamiltonian. Then, for a given set of electrons moving within the field of a set of fixed nuclei, we can find the lowest energy state, called the ground state, of the electrons. This explicit separation of electronic and nuclear parts of the many-body Hamiltonian in (2.2) is the so-called Born–Oppenheimer (BO) approximation⁴⁰. This may be written formally as,

$$\Psi(\mathbf{r}_1, s_1; \dots; \mathbf{r}_{N_e}, s_{N_e}; \mathbf{R}_1, S_1; \dots; \mathbf{R}_{N_n}, S_{N_n}) = \psi_e(\mathbf{r}_1, s_1; \dots; \mathbf{r}_{N_e}, s_{N_e}) \otimes \psi_n(\mathbf{R}_1, S_1; \dots; \mathbf{R}_{N_n}, S_{N_n}), \quad (2.4)$$

where ψ_e and ψ_n are the electronic and nuclear parts of the wavefunction, respectively. The electronic motion can be solved first, calculate the energy of the system in that configuration, and later, compute for the nuclear part in two distinguishable stages. Due to this simplification, the many-body Hamiltonian of (2.2) may be rewritten as a purely electronic Hamiltonian which only depends parametrically on the nuclear coordinates, resulting in

$$\hat{H}_e = - \sum_{i=1}^{N_e} \frac{1}{2} \nabla_{\mathbf{r}_i}^2 + \sum_{i=1}^{N_e} \sum_{j=i+1}^{N_e} \frac{1}{|\mathbf{r}_i - \mathbf{r}_j|} + V_{ext}^{\mathbf{R}_1, \dots, \mathbf{R}_{N_n}}(\mathbf{r}_1, \dots, \mathbf{r}_{N_e}), \quad (2.5)$$

where the external potential V_{ext} includes interactions of the electrons with any external fields or sources. For example, through \hat{V}_{en} we can model the nuclei electromagnetic interaction with the electrons, and this is accounted in the external potential term, V_{ext} . In this way the electronic wavefunction depends only parametrically on the "frozen" nuclear positions, \mathbf{R}_J . Accordingly, the "frozen-nuclei" time-independent Schrödinger equation is

$$\hat{H}_e \psi_e(\mathbf{r}_1, s_1; \dots; \mathbf{r}_N, s_N) = \varepsilon(\mathbf{R}_1, S_1; \dots; \mathbf{R}_{N_n}, S_{N_n}) \psi_e(\mathbf{r}_1, s_1; \dots; \mathbf{r}_{N_e}, s_{N_e}). \quad (2.6)$$

Equation 2.6 is one solution of a collection $\{\psi_e\}$ with eigenvalues $\{\varepsilon\}$. Each value correspond to a solution of the electronic potential energy of the complete system. Neglecting the kinetic energy of the nuclei, we obtain

$$\begin{aligned} \hat{H}_e \Psi &= \hat{H}_e \psi_n(\mathbf{R}_1, S_1, \dots, \mathbf{R}_{N_n}, S_{N_n}) \psi_e(\mathbf{r}_1, s_1, \dots, \mathbf{r}_{N_e}, s_{N_e}) \\ &= \psi_n(\mathbf{R}_1, S_1, \dots, \mathbf{R}_{N_n}, S_{N_n}) \hat{H}_e \psi_e(\mathbf{r}_1, s_1, \dots, \mathbf{r}_N, s_N) \\ &= \varepsilon(\mathbf{R}_1, S_1, \dots, \mathbf{R}_{N_n}, S_{N_n}) \Psi. \end{aligned} \quad (2.7)$$

In this way we may completely decouple the electronic and nuclear parts of the Hamiltonian. Moreover, the much more massive nuclei may be essential treated as classical point particles to a high degree of accuracy. Henceforth, we will use \hat{H} , ψ , and E when referring to the electronic Hamiltonian \hat{H}_e , wavefunction ψ_e , and eigenenergies ε . Although the many-body electronic wave function provides all the information needed, its exact calculation can only be performed for a few atoms.

2.1.3 Periodic systems

In a physical system, such as a solid or a molecule, the number of electrons can be an obstacle to obtaining a physical description of the system, due to the correlated nature of electrons. This problem may be reformulated

using a periodic Schrödinger equation. In the following we shall consider a system of one coordinate \mathbf{r} for notational convenience, however this derivation may be easily extended to a many-body wave function as well. Let us define the shape of a cell that is repeated periodically in space in a material, the supercell, using primitive lattice vectors $\mathbf{a}_1, \mathbf{a}_2, \mathbf{a}_3$. Felix Bloch⁴¹ stated that the electronic wavefunction for any system with a periodic potential, i.e., lattice, may be expressed as a sum of plane waves products, by the same periodicity as the lattice. Mathematically,

$$\psi_{n,\mathbf{k}}(\mathbf{r}) = e^{i\mathbf{k}\cdot\mathbf{r}} u_{n,\mathbf{k}}(\mathbf{r}), \quad (2.8)$$

where \mathbf{k} is a wavevector within the first Brillouin zone (BZ) and $u_{n,\mathbf{k}}(\mathbf{r})$ is a function with the same periodicity in space as the supercell. That is, $u_{n,\mathbf{k}}(\mathbf{r} + \mathbf{R}_n) = u_{n,\mathbf{k}}(\mathbf{r})$, where \mathbf{R}_n is a lattice vector of the form $\mathbf{R}_n = n_1 \mathbf{a}_1 + n_2 \mathbf{a}_2 + n_3 \mathbf{a}_3$ for integers $\mathbf{n} \equiv \{n_1, n_2, n_3\}$. This theorem means that it is possible to solve a Schrödinger equation for each value of \mathbf{k} separately. This yields a relation of correspondence: if the system is periodic, there should also exist a periodic external potential which is also invariant under the translation \mathbf{R}_n ^{42 41},

$$v_{ext}(\mathbf{r} + \mathbf{R}_n) = v_{ext}(\mathbf{r}). \quad (2.9)$$

The unit cell is then a parallelepiped formed by the lattice vectors, and the unit cell's volume is

$$\Omega = |\mathbf{a}_1 \cdot (\mathbf{a}_2 \times \mathbf{a}_3)|. \quad (2.10)$$

The kinetic operator \hat{T}_e and the repulsive electron–electron interaction \hat{V}_{ee} in the many-body Hamiltonian remain unaffected under the translation \mathbf{R}_n . This means that the eigenstates of this Hamiltonian have the same translational symmetry. We may then rewrite (2.8) and (2.9) as

$$\left[-\frac{1}{2} \nabla_{\mathbf{r}}^2 + v_{ext}(\mathbf{r}) \right] \psi_{n,\mathbf{k}}(\mathbf{r}) = \varepsilon_{n,\mathbf{k}} \psi_{n,\mathbf{k}}(\mathbf{r}), \quad (2.11)$$

here, the wavefunction $\psi_{n,\mathbf{k}}(\mathbf{r})$ satisfy Bloch's theorem in all the reciprocal space.

2.1.4 Reciprocal space

In the same way that we defined primitive lattice vectors $\mathbf{a}_1, \mathbf{a}_2$ and \mathbf{a}_3 in real space, we may define their representation in reciprocal space as

$$\mathbf{b}_i = 2\pi \frac{\mathbf{a}_j \times \mathbf{a}_k}{\Omega}, \quad (2.12)$$

where $i, j, k \in \{1, 2, 3\}$ and $i \neq j \neq k$. These \mathbf{b}_i form a complete set of three primitive reciprocal lattice vectors.

In (2.11), the wavevector \mathbf{k} reflects the periodicity of the system and the integer n corresponds to independent eigenstates of the system at different eigenvalues. Moreover, for any wavevector \mathbf{k} within the first BZ, there is a complete set of electronic bands n . For example, the electronic band structure for any solid can be computed by considering the eigenvalues $\varepsilon_{n,\mathbf{k}}$, and plotting them across a reciprocal k -space specific path. We may restrict consideration to \mathbf{k}_ℓ

$$\mathbf{k}_\ell = \frac{\ell_1}{N_1} \mathbf{b}_1 + \frac{\ell_2}{N_2} \mathbf{b}_2 + \frac{\ell_3}{N_3} \mathbf{b}_3, \quad \text{with } -\frac{N_i}{2} \leq \ell_i < \frac{N_i}{2}, \quad (2.13)$$

where ℓ_i and N_i are positive integers. By applying these restrictions, we have defined the first BZ in reciprocal space. Since the first BZ covers all the reciprocal unit cell, any \mathbf{k} wavevector outside of these constraints has already been included.

Many properties of a solid can be calculated by the evaluation of integrals over the BZ in reciprocal space. By using a discrete set of \mathbf{k} -points, we can approximate accurately to these integrals⁴³. To illustrate this, the integral of a function $F(\mathbf{k})$ over the BZ may be approximated as

$$\frac{1}{\Omega_{\text{BZ}}} \int_{\text{BZ}} F(\mathbf{k}) d\mathbf{k} \approx \sum_{\mathbf{k}} w_{\mathbf{k}} F(\mathbf{k}), \quad (2.14)$$

here Ω_{BZ} is the definition of the BZ volume, and $w_{\mathbf{k}}$ is the weight in the sum of the k -point \mathbf{k} . Approximately, the integral is similar to the weighted finite sum over the \mathbf{k} -points of the first BZ. It is important to note that through the application of the symmetries of the unit cell, e.g., time-reversal symmetry, we may remove equivalent k -points from the sum by appropriately adjusting their weights $w_{\mathbf{k}}$. The resulting unit cell is the so-called irreducible Brillouin zone (IBZ). For highly symmetric systems, we may significantly reduce the number of k -points for which we need to perform calculations.

2.1.5 The Hohenberg–Kohn theorem

The task of computing the solution for all the electrons in a solid or a molecule is computationally expensive. A solution to this problem is by calculating the total energy as a function of the electron density at one position \mathbf{r} , i.e., 3 variables, rather than a wave function dependent on N positions \mathbf{r}_i , i.e., N variables. The electron number density $n(\mathbf{r})$ for a spin-paired system in the limit $T \rightarrow 0$ may be written in terms of the individual electron wavefunctions $\psi_i(\mathbf{r})$ as

$$n(\mathbf{r}) = 2 \sum_{i=1}^{N_e/2} \psi_i^*(\mathbf{r}) \psi_i(\mathbf{r}), \quad (2.15)$$

where the summation is over all $N_e/2$ doubly-occupied wavefunctions, that is, the probability of an electron occupying an individual wave function $\psi_i(\mathbf{r})$ being located at position \mathbf{r} . The factor of two appears because all electrons have been assumed to doubly occupy each eigenstate of the Hamiltonian. This comes from the Pauli exclusion principle, which states that at most two electrons of opposite spin, i.e., \uparrow and \downarrow , may occupy each eigenstate of the system⁴⁴. The first Hohenberg–Kohn (HK) theorem, asserts that there exists a one-to-one mapping between the ground-state wave function and the ground-state electron density⁴⁵ of a solid:

Theorem 1. The ground state of an interacting many-particle system with a given fixed inter-particle interaction is a unique functional of its electron density $\rho(\mathbf{r}) = -n(\mathbf{r})$.

The ground-state electron density then determines by itself all physical properties, including the wave function and the eigenenergies, of the ground state. In this way, the ground-state energy E is a functional of the electron density as $E[n(\mathbf{r})]$, which may be obtained by knowing the inter-particle interaction or the external potential $v_{\text{ext}}(\mathbf{r})$. The proof of this theorem can be found in the Ref. 46. As the ground state functional is unique for the ground state

density, $n_0(\mathbf{r})$, we can assert that

$$|\psi_0\rangle = |\psi[n_0]\rangle. \quad (2.16)$$

Such a functional dependence allows one to compute any ground state observable \hat{O} as a density functional,

$$O[n] \equiv \langle \psi[n] | \hat{O} | \psi[n] \rangle. \quad (2.17)$$

The ground state energy, may be expressed as,

$$E[n] \equiv \langle \psi[n] | \hat{H} | \psi[n] \rangle = F[n] + \int d^3\mathbf{r} v_{ext}(\mathbf{r})n(\mathbf{r}), \quad (2.18)$$

where $F[n] \equiv \langle \psi[n] | (\hat{T}_e + \hat{V}_{ee}) | \psi[n] \rangle$,

as the most relevant density functional for the electronic description of a system. In (2.18) $F[n]$ represents the universal part of the ground state energy functional, and v_{ext} enters as an input to $E[n]$. Another fundamental part of density functional theory (DFT) describes the minimum principle of the ground state energy functional $E[n]$. The second HK theorem defines this important property of the functional:

Theorem 2. "The electron density that minimizes the energy of the overall functional is the true electron density corresponding to the full solution of the Schrödinger equation"⁴⁵.

As the theorem states, all electronic densities $n'_0(\mathbf{r}) \neq n_0(\mathbf{r})$, where n_0 is defined as its ground state density corresponding to external potential v_{ext} ,

$$E[n_0] < E[n'_0] \iff E_0 = \min_{n \in \mathcal{N}} E[n], \quad (2.19)$$

here \mathcal{N} is number of all the sets set of all ground state densities for each v_{ext} . This definition is a consequence of the so called Ritz variational principle, that refrains that the ground state $|\psi'_0\rangle$ for the density n'_0 does not match to $|\psi_0\rangle$. For these reasons, it is possible to vary the electron density $n'_0(\mathbf{r})$ until the energy of the functional is minimized, reaching the ground state electron density $n_0(\mathbf{r})$.

The functional $E[n]$ is only defined for the domain restricte to the electronic densities in \mathcal{N} , as obtained by solving (2.6)⁴⁷. The energy functional can be broken into four main contributions

$$E[n] = T[n] + E_H[n] + E_{ext}[n] + E_{xc}[n], \quad (2.20)$$

here, $T[n]$ is kinetic energy functional of each n , $E_H[n]$ is Hartree interaction energy functional or the so called self interaction contribution⁴⁸, $E_{ext}[n]$ is the external potential energy functional, and $E_{xc}[n]$ is the exchange and correlation (xc) energy functional. The xc functional accounts for the complicated effects of the interactions not present in T , E_H , or E_{ext} .

2.1.6 Self-consistent Kohn–Sham system

The idea of DFT is to introduce a one-electron Schrödinger equation of a system with non-interacting electrons that has the same electron density as the real system. In other words, to create a direct mapping between the interacting

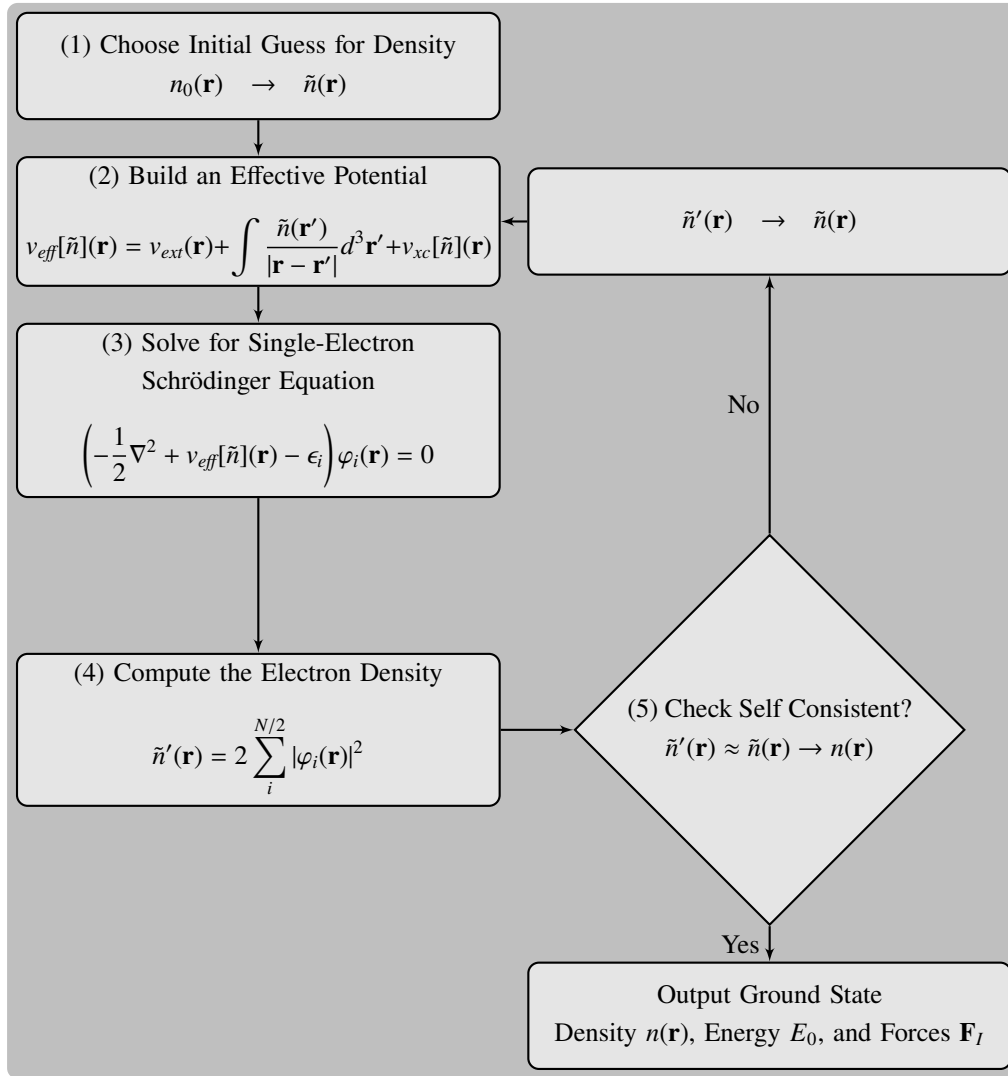


Figure 2.1: KS self-consistent scheme. Adapted from Ref. 50.

many-body problem and a suitable non-interacting system. We call the latter the Kohn–Sham (KS) system, as in Ref. 49. The ground state density $n_0(\mathbf{r})$, as well as its corresponding energy E_0 and nuclear forces \mathbf{F}_I may be found by using self consistent field equations and density functional methods, . The KS scheme has five self-consistent steps:

1. Define an initial, trial guess for the electron density $\tilde{n}(\mathbf{r})$.

2. The effective potential

$$v_{eff}[\tilde{n}](\mathbf{r}) = v_{ext}(\mathbf{r}) + \int \frac{\tilde{n}(\mathbf{r}')}{|\mathbf{r} - \mathbf{r}'|} d^3\mathbf{r}' + v_{xc}[\tilde{n}](\mathbf{r}), \quad (2.21)$$

is calculated as a function of $\tilde{n}(\mathbf{r})$, here the first term correspond to the external potential for the fixed nuclei $v_{ext}(\mathbf{r})$, and the second and third term corresponds to the Hartree potential and the xc potential v_{xc} , respectively.

3. The non-interacting picture of Schrödinger equation is solved to obtain the KS wavefunctions φ_i . Then effective potential v_{eff} is used for computing the trial density $\tilde{n}(\mathbf{r})$:

$$\left(-\frac{1}{2}\nabla^2 + v_{eff}[\tilde{n}](\mathbf{r}) - \epsilon_i \right) \varphi_i(\mathbf{r}) = 0. \quad (2.22)$$

4. The newly computed KS electron number density $\tilde{n}'(\mathbf{r})$ is obtained from the KS wavefunctions of the last step. Assuming the system is spin-paired, the electronic number density may be computed by summing the $N/2$ lowest energy doubly-occupied wavefunctions $\varphi_i(\mathbf{r})$

$$\tilde{n}'(\mathbf{r}) = 2 \sum_{i=1}^{N/2} |\varphi_i(\mathbf{r})|^2. \quad (2.23)$$

5. Compare the outputted KS electron number density $\tilde{n}'(\mathbf{r})$ with the electron density used in solving the KS single electron calculation $\tilde{n}(\mathbf{r})$. Steps (2), (3), and (4) are repeated self-consistently until the density is converged, that is, both outputted and inputted densities are approximately equal within a defined accuracy. Once this is achieved, the outputted self-consistent electron density and eigenenergies ϵ_i are those of the ground state of the system, within the prescribed accuracy. This cycle is also shown in Fig. 2.1.

The KS wavefunctions φ_i yield the electron density of the fully-interacting system and $\epsilon_{N/2}$, the eigenvalue corresponding to the highest occupied molecular orbital (HOMO), is the ionization energy. However, the KS wavefunctions and other eigenenergies themselves have no direct theoretical connection to the wavefunctions and eigenenergies of the fully interacting system. At last, the ground state energy E_0 can be used from KS scheme results to solve for the electronic properties of the system:

$$E_0 = \sum_{i=1}^{N/2} \epsilon_i + E_{xc}[n] - \int v_{ext}(\mathbf{r})n(\mathbf{r})d^3\mathbf{r} + \frac{1}{2} \iint \frac{n(\mathbf{r})n(\mathbf{r}')}{|\mathbf{r} - \mathbf{r}'|} d^3\mathbf{r}d^3\mathbf{r}'. \quad (2.24)$$

The results of Kohn, Hohenberg, and Sham are remarkable for calculating the ground state of the real system by finding a self-consistent solution to a set of single-particle equations. However, the critical complication comes from the fact that the xc potential v_{xc} is not known for many body systems.

2.1.7 Spin-polarized density functional theory

For non-interacting electrons, if an induced magnetic field is applied, it generates a coupling to the electron spin and the electronic orbital current. To describe the magnetic properties of metals and even organic materials, a

spin-DFT framework is required withing the KS scheme⁵¹. This method allows us to predict and understand the band magnetism of electrons in molecules at finite temperature. In this DFT implementation, the spin up (\uparrow) and spin down (\downarrow) densities $n^{\uparrow,\downarrow}$ are expressed in terms of the KS spin orbitals,

$$n^{\uparrow,\downarrow}(\mathbf{r}) = \sum_{i=1}^{(N_e \pm \mu)/2} |\psi_{i,\uparrow,\downarrow}(\mathbf{r})|^2, \quad (2.25)$$

where N_e is the number of electrons and μ is the total magnetic moment. The KS equations in term of the orbitals may then be written as,

$$\left[-\frac{1}{2}\nabla_{\mathbf{r}}^2 + v_{eff}^{\uparrow,\downarrow}(\mathbf{r}) \right] \psi_{n,\mathbf{k}}^{\uparrow,\downarrow}(\mathbf{r}) = \varepsilon_{n,\mathbf{k}}^{\uparrow,\downarrow} \psi_{n,\mathbf{k}}^{\uparrow,\downarrow}(\mathbf{r}), \quad (2.26)$$

for each spin eigenenergy $\varepsilon_{n,\mathbf{k}}^{\uparrow,\downarrow}$. The form of the spin dependent effective potential is, then

$$V_{eff}^{\uparrow,\downarrow} = \frac{1}{2} \int \frac{n^{\uparrow,\downarrow}(\mathbf{r}')}{|\mathbf{r} - \mathbf{r}'|} d\mathbf{r}' + V_{ext}^{\uparrow,\downarrow}(\mathbf{r}) + V_{xc}^{\uparrow,\downarrow}(\mathbf{r}) \quad (2.27)$$

where $V_{xc}^{\uparrow,\downarrow}(\mathbf{r})$ and $V_{ext}^{\uparrow,\downarrow}(\mathbf{r})$ are the xc and external potential, respectively. In an external magnetic field H , the external potential V_{ext} contains a magnetic field term $\pm(\mu_B H)$ that, if is negative (positive), it will favor energetically the spin up (down) electron compared to the minority spin down (up) electrons. The xc potential $V_{xc}^{\uparrow,\downarrow}$ is then defined as,

$$V_{xc}^{\uparrow,\downarrow}(\mathbf{r}) = \frac{\delta E_{xc}[n^{\uparrow}(\mathbf{r}), n^{\downarrow}(\mathbf{r})]}{\delta n^{\uparrow,\downarrow}(\mathbf{r})}. \quad (2.28)$$

The xc energy can have different values for each spin species, even without an external magnetic field. The total functional or Hohenberg–Kohn–Sham spin-density functional is defined as,

$$E[n^{\uparrow}, n^{\downarrow}] = T[n^{\uparrow}] + T[n^{\downarrow}] + \frac{1}{2} \iint \frac{n^{\uparrow}(\mathbf{r})n^{\uparrow}(\mathbf{r}')}{|\mathbf{r} - \mathbf{r}'|} d\mathbf{r}d\mathbf{r}' + \frac{1}{2} \iint \frac{n^{\downarrow}(\mathbf{r})n^{\downarrow}(\mathbf{r}')}{|\mathbf{r} - \mathbf{r}'|} d\mathbf{r}d\mathbf{r}' \\ + \frac{1}{2} \iint \frac{n^{\uparrow}(\mathbf{r})n^{\downarrow}(\mathbf{r}') + n^{\downarrow}(\mathbf{r})n^{\uparrow}(\mathbf{r}')}{|\mathbf{r} - \mathbf{r}'|} d\mathbf{r}d\mathbf{r}' + \int V_{ext}^{\uparrow}(\mathbf{r})n^{\uparrow}(\mathbf{r})d^3\mathbf{r} + \int V_{ext}^{\downarrow}(\mathbf{r})n^{\downarrow}(\mathbf{r})d^3\mathbf{r} + E_{xc}[n^{\uparrow}(\mathbf{r}), n^{\downarrow}(\mathbf{r})], \quad (2.29)$$

where $T[n^{\uparrow,\downarrow}]$ is the kinetic functional, the next terms are the Coulomb functionals, the interaction energy with the effective potential V_{eff} and the xc energy for each spin state.

In order to solve the KS scheme, we just need to obtain the minimum of the functional in Eqs. 2.29, 2.26, by an iterative scheme as in Fig. 2.1 to find the ground state spin matrix that yields to the ground state-energy, and find each set of spin eigenenergies^{52,53}.

2.1.8 Exchange and correlation functionals

Since the HK theorem guarantees the existence of v_{xc} , it could be numerically approximated to calculate the ground state energy, e.g., by stochastic methods⁵⁴.

Local density approximation

One of the first xc energy functionals, proposed originally by Slater⁵⁵ to simplify the Hartree-Fock (HF) calculations and first optimized by Perdew and Zunger⁵⁶, is the local density approximation (LDA) xc functional. They considered a homogeneous electron gas (HEG), so that the electron density is only a function of the density observed at its position. The LDA xc-energy density is then computed as,

$$E_{xc}^{\text{LDA}}[n] = \int \epsilon_{xc}^{\text{HEG}}(n_0 = n(\mathbf{r})) d^3 \mathbf{r}. \quad (2.30)$$

The LDA is simply a function of the local density, so it can be easily used in the KS scheme⁴⁷,

$$v_{xc}^{\text{LDA}}(\mathbf{r}) = \frac{\delta E_{xc}^{\text{LDA}}[n]}{\delta n(\mathbf{r})}. \quad (2.31)$$

Physically, the v_{xc}^{LDA} has an extremely short range due to its local description. Despite considering only a completely homogeneous electron density in its construction, it has been surprisingly successful in reproducing experimental results. The LDA itself respects the sum rule of one electron being excluded from the surroundings of other electrons. Besides this, LDA benefits from a fortuitous error cancellation. LDA generally overestimates the correlation energy and underestimates the exchange energy, but in such a way that these errors tend to cancel each other out.

However, LDA is known to have several disadvantages. For example, LDA tends to overestimate molecular binding⁵⁷, yielding upshifts in the orbital energy spectrum⁵⁸, underestimate band gaps⁵⁹, among others. Here a band gap is defined as the energy difference in energy between the states associated to the conduction band minimum (CBM) and the valence band maximum (VB).

Generalized gradient approximation

For a more complete description of non-homogeneities in the electron density, a gradient-dependent semi-local approximation is often used. The generalized gradient approximation (GGA) is based on slow density variations around the electron coordinates. The GGA exchange functional generally takes the form⁶⁰,

$$E_x^{\text{GGA}}[n] = \int \epsilon_x^{\text{HEG}}(n_0 = n(\mathbf{r})) F_x[s(\mathbf{r})] d^3 \mathbf{r}, \quad (2.32)$$

where ϵ_x^{HEG} is the exchange energy density of a HEG ($\sim n^{4/3}$), $n(\mathbf{r})$ is the electron number density, F_x is an enhancement factor, and s is the dimensionless generalized density gradient,

$$s = \frac{|\nabla n|}{2k_F n}, \quad (2.33)$$

with $k_F = (3\pi^2 n)^{1/3}$. Eq. (2.32) is clearly spin-unpolarized, although a spin-polarized formulation may be derived⁶¹. The enhancement factor can be used to recover the HEG limit as

$$F_x[s] = 1 + \mu s^2 + \dots \quad (s \rightarrow 0). \quad (2.34)$$

Then, the correlation functional can be computed as HEG limit states, as

$$E_c^{\text{GGA}}[n] = \int n(\mathbf{r}) \left(\epsilon_c^{\text{HEG}}(n_0 = n(\mathbf{r})) + \frac{\pi}{8k_F} \beta \frac{|\nabla n(\mathbf{r})|^2}{n(\mathbf{r})^2} + \dots \right) d^3\mathbf{r}, \quad (2.35)$$

where ϵ_c^{HEG} is the correlation energy density of the HEG and β is a coefficient for tuning the gradient approximation. Originally, GGA functionals were empirical, obtained by fitting experimental data, so that their applicability was limited to specific systems. However, the gradient corrected nonlocality functional for a generalized system, the Perdew-Burke-Ernzerhof xc functional (PBE), has a general applicability, making it suitable for DFT calculations of systems in general⁶¹.

Perdew-Burke-Ernzerhof xc functional

PBE takes advantage over the LDA since it includes heterogeneity by adding two corrections by using the generalized gradient functional. The PBE is defined by the two fundamental parameters empirically,

$$\mu = 0.21951 \text{ and } \beta = 0.0066725. \quad (2.36)$$

As a result, PBE reduces significantly the over binding of the local spin-density approximation (LSDA) but overestimates lattice constants. The PBE xc functional has been used throughout this thesis, and further literature and benchmarking of PBE may be found in Refs 62 and 63.

Perdew-Burke-Ernzerhof xc functional for solids

Perdew-Burke-Ernzerhof xc functional for solids (PBEsol) is a revised version of PBE-GGA that incorporates additional equilibrium properties of dense solids and their surfaces. Specifically, PBEsol has been designed to provide an improved description of lattice constants over PBE. To do so the main PBE parameters were modified,

$$\mu = \mu_{GE} = 0.1235 \text{ and } \beta = 0.046, \quad (2.37)$$

where μ_{GE} provides a more accurate gradient expansion for slowly varying electronic densities. This functional reduces the dependence on error cancellation by providing accurate xc energies of surfaces. A number of tests for solids have been performed in Ref. 64.

2.2 Representations of the Kohn–Sham wavefunctions

A wavefunction is a quantum description of the “state” of a system. As an element of a Hilbert space, it belongs to a vector space with an inner product. Therefore, a linear combination of wavefunctions $\{\phi_i\}$ is also a quantum description of a given system, and an appropriate basis set. In such a basis set an arbitrary wave function $\psi(\mathbf{r})$ may be written as,

$$\psi(\mathbf{r}) = \sum_i c_i \phi_i(\mathbf{r}), \quad (2.38)$$

where $c_{n,i}$ are the wave function coefficients, which must satisfy the normalization condition $\sum_{ij} c_i^* c_j \langle \phi_i | \phi_j \rangle = 1$, or $\sum_i |c_i|^2 = 1$ when the basis functions are orthonormal, i.e., $\langle \phi_i | \phi_j \rangle = \delta_{ij}$. In practice, the summation over elements of the basis is truncated to find the solution of the KS equation, yielding a finite density matrix used to solve the eigenvalue problem.

DFT calculations generally employ one of three methods for representing the periodic part $u_{n,\mathbf{k}}(\mathbf{r})$ of the KS wavefunctions $\varphi_{n,\mathbf{k}}(\mathbf{r})$ and the electron number density $n(\mathbf{r})$: finite difference (FD), plane wave (PW), or linear combination of atomic orbitals (LCAO). FD representations calculate these functions on a finite real space grid point mesh, employing higher-order interpolation to obtain their values at intermediate points. A PW representation instead uses the discrete Fourier transform to represent these functions in reciprocal space, ensuring they are periodic. Finally, LCAO uses a combination of pre-determined basis sets, typically including hydrogenic-like orbitals localized at each nuclei to represent these functions.

Since LCAO is the basis set used in the Thesis, it will be expanded further in the next sections.

2.2.1 Plane wave

For periodic systems, it is often convenient to represent the periodic part of the wavefunctions, $u_{n,\mathbf{k}}(\mathbf{r})$, from Bloch's theorem (2.8), using its discrete Fourier transform from in reciprocal space as functions of \mathbf{k} rather than in real space as functions of \mathbf{r} . For these PW calculations we employ the reciprocal translation vector as $\mathbf{G}_m = m_1 \mathbf{b}_1 + m_2 \mathbf{b}_2 + m_3 \mathbf{b}_3$ for any integers m_1, m_2 , and m_3 , where $\mathbf{m} = \{m_1, m_2, m_3\}$. Furthermore, the periodicity of $u_{\mathbf{k}}(\mathbf{r})$ means that the plane wave in (2.8) can be expanded in term of a special set of PWs, so that the wavefunction $\psi_{n,\mathbf{k}}(\mathbf{r})$ may be expanded as,

$$\psi_{n,\mathbf{k}}(\mathbf{r}) = \sum_{\mathbf{G}_m} c_{\mathbf{k}+\mathbf{G}_m} e^{i(\mathbf{k}+\mathbf{G}_m)\cdot\mathbf{r}}, \quad (2.39)$$

i.e., employing a discrete Fourier transform. Solving for the kinetic energy in (2.11) we obtain

$$E_{\mathbf{k},\mathbf{G}_m} = 2\pi^2 |\mathbf{k} + \mathbf{G}_m|^2, \quad (2.40)$$

where \mathbf{k} is the wave vector describing long-range electronic behavior and \mathbf{G}_m is the reciprocal translational vector, which describes local behavior within the BZ. The larger the number of \mathbf{G}_m we include, the finer the description of the wavefunction will be. \mathbf{G}_m allows you to described local behaviour, and the k vector allows us to assign a long-range vectorial description to the electron's eigenvectors, normally larger that the unit cell. It is reasonable to expect that the lower energy solutions will be the most physically meaningful. For this reason, we employ a cut-off energy E_{cut} for the plane wave expansion of the wavefunctions, defined as,

$$E_{cut} = 2\pi^2 G_{cut}^2. \quad (2.41)$$

The infinite sum in (2.39) then reduces to

$$\psi_{n,\mathbf{k}}(\mathbf{r}) = \sum_{|\mathbf{G}_m+\mathbf{k}| < G_{cut}} c_{\mathbf{k}+\mathbf{G}_m} e^{i(\mathbf{k}+\mathbf{G}_m)\cdot\mathbf{r}}. \quad (2.42)$$

In general, a finite number of sampling points in the first BZ is required for performing calculations using Bloch waves within KS scheme. Each orbitals vary smoothly with respect to the set of \mathbf{k} chosen, and calculations need to be converged for each one of the sampled \mathbf{k} -points. We employ a Monkhorst-Pack sampling⁶⁵ of special⁶⁶ k -points as it is an unbiased method to select these points in an homogeneous mesh

$$\mathbf{k}(n_1, n_2, n_3) = \sum_{i=1}^3 \frac{2n_i - N_i - 1}{2N_i} \mathbf{b}_i, \quad (2.43)$$

where $n_i \in \{1, \dots, N_i\}$ and N_i corresponds to the number of points in the \mathbf{b}_i direction.

2.2.2 Linear combination of atomic orbitals

A LCAO representation is based on the premise that molecular orbitals can be expressed as a quantum superposition of atomic orbitals⁶⁷, ϕ_ν , so that

$$\psi_{n,\mathbf{k}}(\mathbf{r}) = \sum_{I=1}^{N_n} \sum_{\nu=1}^{\nu_I} c_{n,\mathbf{k}}^{I,\nu} e^{i\mathbf{k}\cdot\mathbf{r}} \phi_\nu(\mathbf{r} - \mathbf{R}_I), \quad (2.44)$$

where N_n is the number of nuclei, ν_I is the number of basis functions ϕ_ν and \mathbf{R}_I is the position of the I th atom. LCAO allows one to define the wave function locally in a natural way, making them ideal representations for transport calculations. Although the use of LCAO cannot be systematically converged to the ground state, LCAO has proven to be quite reliable and effective for describing systems with large numbers of atoms per unit cell⁶⁸, since the computational cost scales only with the system size and is independent of any vacuum regions⁶⁹. Furthermore, the real advantage of LCAO is the use of known functions and far fewer unknown coefficients compared to PW methods⁷⁰. The DFT package used herein, grid-based projector augmented wave method code (GPAW)⁷¹, offers the possibility to work with LCAO basis sets and their generation⁷². A mathematical formulation of these atomic orbitals, $\phi_{\nu=|n,l,m\rangle}(\mathbf{r})$, can be defined as the product of characteristic radial function $R_{nl}(r)$ and spherical harmonics $Y_{lm}(\theta, \varphi)$ as

$$\phi_{nlm}(\mathbf{r}) = R_{nl}(r)Y_{lm}(\theta, \varphi) \quad (2.45)$$

where $\mathbf{r} = \{r, \theta, \varphi\}$ are the spherical coordinates of the hydrogenic-like particle (2.38), summation index ν runs over n , l , and m quantum numbers of the state. These basis functions are computed by solving each of the all-electron KS equations^{73,74}.

2.2.3 Basis sets generation for linear combination of atomic orbitals

The basis functions $\phi_{nlm}(\mathbf{r})$ of (2.45) are atom-centered orbitals. Hamiltonians and overlap matrices may be generated using localized radial functions, that is, employing a radial cutoff for long-range overlaps^{74,75}. For example, typical radial cutoffs for LCAO calculations are $r_{cut} \approx 6 \text{ \AA}$. The basis orbitals of single- ζ (SZ) basis sets, $R_{nl}(r)$, are generated for each valence state $|nl\rangle$ by solving the all-electron KS equations for an isolated atom using a confining potential $|nl\rangle$ is used. Double- ζ (DZ) and triple- ζ (TZ) basis sets use extra basis functions, but with the same angular momentum for each valence state to improve their radial flexibility. To improve their description of unoccupied states, basis

functions with the angular momentum l of the lowest unoccupied molecular orbital (LUMO) are also generated, often implemented as Gaussian-type functions, as implemented in the Spanish initiative for electronic simulations with thousands of atoms code (SIESTA). Such basis sets may be improved through the inclusion of polarization functions that have higher angular momentum l functions, e.g., single- ζ polarized (SZP) or double- ζ polarized (DZP). Each angular momentum $l + 1$, are included in the polarized basis sets, where l is the angular momentum of the HOMO. As generated in the GPAW package, the LCAO basis set for C includes two confined orbitals, two split-valence waves, and one d -type Gaussian polarization function⁷¹. This basis set is locally orthogonal but non-orthogonal between neighboring atomic basis sets. This means one must calculate overlaps between the atoms,

$$\int \phi_{\nu}(\mathbf{r} - \mathbf{R}_I) \phi_{\nu'}(\mathbf{r} - \mathbf{R}_J) d^3 \mathbf{r}, \quad (2.46)$$

but not with in the same atom

$$\int \phi_{\nu}(\mathbf{r} - \mathbf{R}_I) \phi_{\nu'}(\mathbf{r} - \mathbf{R}_I) d^3 \mathbf{r}. \quad (2.47)$$

2.2.4 Projector augmented wave method

In a real material, wave functions behave differently depending on the region of space. For example, in the interaction or bonding region they are quite smooth, whereas near nuclei they oscillate rapidly. A solution to this difficulty is to “cut” or partition the wave function into two parts. Specifically, by employing a partial wave expansion within an atom-centered sphere and convenient functions outside the sphere. The partial wave and envelope functions are matched with derivative and direct evaluation at the sphere radius. The all-electron (AE) wave functions may be transformed into smooth pseudo (PS) wavefunctions in a new PS Hilbert space. We may define a linear operator $\mathcal{T}\hat{\mathcal{T}}$ that maps from a PS wave function $|\tilde{\psi}\rangle$ to the AE wave function $|\psi\rangle$,

$$|\psi\rangle = \hat{\mathcal{T}}|\tilde{\psi}\rangle. \quad (2.48)$$

For any operator \hat{O} , its expectation value satisfies

$$\langle \hat{O} \rangle = \langle \psi | \hat{O} | \psi \rangle = \langle \tilde{\psi} | \hat{\mathcal{T}}^\dagger \hat{O} \mathcal{T} | \tilde{\psi} \rangle, \quad (2.49)$$

in the PS Hilbert space. Since we require a linear transformation, we choose a particular transformation within some augmentation region Ω_R enclosing the I th atom a

$$\hat{\mathcal{T}} = \sum_{I=1}^{N_n} \hat{\mathcal{T}}_{\mathbf{R}_I}. \quad (2.50)$$

This means that outside of the augmentation region the AE and PS wave functions should coincide. Then, for a particular $T_{\mathbf{R}_I}$, we define projector functions for the I th atom $\tilde{p}_{\nu,I}$ that are localized in the augmentation function and fulfill

$$\sum_{I=1}^{N_n} \sum_{\nu=1}^{v_I} |\tilde{\chi}_{\nu,I}\rangle \langle \tilde{p}_{\nu,I}| = 1, \quad (2.51)$$

where $|\tilde{\chi}_{v,l}\rangle$ forms a partial wave expansion of the PS wave functions

$$|\tilde{\psi}_v\rangle = |\tilde{\chi}_{v,l}\rangle\langle\tilde{p}_{v,l}|\tilde{\psi}\rangle. \quad (2.52)$$

The transformation of the projector augmented wave (PAW) formalism for valence wave functions is then

$$\hat{\mathcal{T}} = 1 + \sum_{l=1}^{N_n} \sum_{v=1}^{v_l} (|\chi_{v,l}\rangle - |\tilde{\chi}_{v,l}\rangle)\langle\tilde{p}_l^a|. \quad (2.53)$$

On the other hand, core electron wave functions transform from AE Hilbert space to PS Hilbert space similarly to valence wave functions. The frozen-core approximation for a core state c may be expressed as

$$|\psi_{c,l}\rangle = |\tilde{\psi}_{c,l}\rangle + |\phi^a\chi_{c,l}\rangle - |\tilde{\psi}_{c,l}\rangle = |\chi_{c,l}\rangle. \quad (2.54)$$

In this case no projector is needed since the wave functions are the same as the partial waves. In this sense, a PS potential can also be obtained by solving the KS equation for the PS wave function. This enhancement, by separating the core states and valence states, allows their proper physical description and is useful for the computation of the Coulomb potential^{76,77}, and also allows one to work with the all-electron wavefunctions and density by using the projectors. Another advantage of using PAW, is that it tracks the smooth and highly oscillatory wavefunction inside the core, by considering spherical symmetry. The DFT code used, GPAW⁷¹, employs the PAW formalism for all its calculations.

2.3 Analytical Tight binding models

As we reviewed in Section 2.2.3, LCAO is a standard model used for solving periodic potential problems, as the basis set is formed with Bloch Waves (2.8). The method used here was first described by Bloch⁷⁸, and simplified significantly by Slater and Koster⁷⁹, as an interpolation method instead of a rigorous calculation. The first simplification is made by considering only the atomic orbitals whose energies are close to the main electronic states we are interested in. For example, for organic molecules, $1s$ orbitals can be neglected, by only considering $2s$ and $2p$ orbitals since these orbitals have the main role in the valence and conduction bands of the system. By fitting certain energies and orbital parameters, we can avoid rather large errors due to artifacts without serious difficulties. For this revision, the system of units will be international units. We define a Hamiltonian H as the sum of spherical potentials located in the atom's orbitals. Then the Hamiltonian components are defined as,

$$H_{\mu\nu}^I = \int \psi_{\mu}(\mathbf{r} - \mathbf{R}_i)\hat{H}\psi_{\nu}(\mathbf{r} - \mathbf{R}_j)\mathbf{d}^3\mathbf{r}, \quad (2.55)$$

where $(\mathbf{R}_j, \mathbf{R}_i)$ are the position vector of the atom's orbital $\psi_{\mu}(\mathbf{r} - \mathbf{R}_j)$ and $\psi_{\nu}(\mathbf{r} - \mathbf{R}_i)$. If the orbitals $\psi_{\mu,\nu}$ are orthogonalized Löwdin functions⁸⁰, then only non-vanishing integrals are the ones located in the neighborhood of the given orbital; there are the so-called two-center integrals, or in the literature, Slater–Koster (SK) components^{23,81}. Then, the first, second or third neighbor order may be used, regarding how many constants we want to use to describe the desired physical picture.

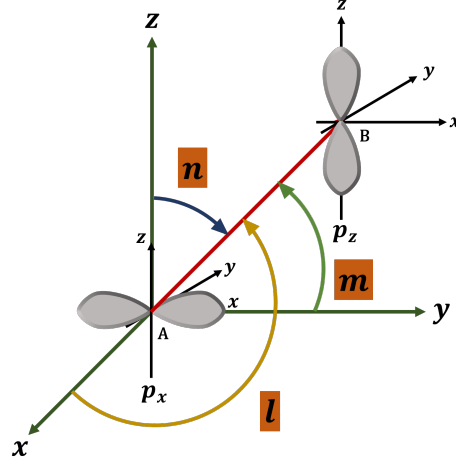


Figure 2.2: SK sides A and B. The SK kinetic overlaps is defined by the three angles $\mathbf{l} = \cos(\alpha)$, $\mathbf{m} = \cos(\beta)$ and $\mathbf{n} = \cos(\gamma)$, defined by the cosine of the angle from the principal axis to the vector joining side A and B.

2.3.1 Slater–Koster components

In practice, the SK component may be computed fairly easily following orthonormality conditions and neglecting far orbital interactions. For example, if the wavefunction ψ is conformed with p orbital, we can express it as a linear combination of orbitals $p_\sigma p_{\pi_\pm}$, where σ is a covalent bond resulting from the formation of a molecular orbital by the end-to-end overlap of atomic orbitals; and π when each atomic orbital type is an orthonormalized Löwdin function. Thus, non-vanishing components of p orbitals are the ones when both ψ_n and ψ_m are of the same type, that is $\sigma - \sigma$, $\pi_+ - \pi_+$ or $\pi_- - \pi_-$.

The integrals can be set up by just considering the direction cosines of the displacement $\mathbf{R}_j - \mathbf{R}_i$ from atom i to j , be l , m and n , as showed in Fig. 2.2. For further reference, all the computations of SK component are derived in Ref. ⁷⁹.

As a matter of simplicity, SK components can be expressed in a rather simple way, by just considering the 3 spatial coordinates of two center sites A and B, such as:

$$H_{A,\mu;A,\mu'} = H_{B,\mu;B,\mu'} = V_{\mu,\mu'} \delta_{\mu,\mu'}, H_{B,\mu;A,\mu'} = H_{A,\mu';B,\mu}^* = \sum_{i=1}^{\gamma} e^{i(\mathbf{R}_j - \mathbf{R}_i) \cdot \mathbf{k}} E_{\mu\mu'}^{ij}, \quad (2.56)$$

where μ, μ' label the orbitals in the site A and B respectively, and $E_{\mu\mu'}^{i,j}$ stands for hopping energy between orbitals and γ is the number of neighbors j . Now, the SK kinetic overlaps are calculated as (see Fig. 2.2),

$$E_{\mu,\mu'}^{ij} = \langle \mu | V | \mu' \rangle = (\hat{n}(\mu_i)^\parallel, \hat{n}(\mu'_j)^\parallel) V_{\mu\mu}^\sigma + (\hat{n}(\mu_i)^\perp, \hat{n}(\mu'_j)^\perp) V_{\mu\mu}^\pi, \quad (2.57)$$

where $V_{\mu\mu}^{\pi,\sigma}$ are the SK parameters, that represent the overlap between orbital $\mu - \mu'$, normally fitted by other more accurate methods. The projections $\hat{n}(\mu_i)^\parallel$ join the two atomic enters R_{ij} and $\hat{n}(\mu_i)^\perp$ projections perpendicular to R_{ij} . Notice that $V_{\mu\mu}^{\pi,\sigma}$ parameters depend strongly on the distance.

2.3.2 Intrinsic spin-orbit coupling

In general, the magnetic moment can be defined as the electric current going around a closed loop⁴². In an atomic system, the spin magnetic moment of an electron is generated by its spin

$$\mu_S = -g_s \mu_B S \quad (2.58)$$

where S is the spin angular momentum operator, μ_B is the Bohr magneton, and g_s is the electron–spin g-factor⁴². In the context of the low dimensional system, spin-orbit coupling (SOC) is a form of the intrinsic effective magnetic field, affected by the spin in its rest frame. Despite not being a true magnetic field because $\mathbf{B} = 0$, it can generate spin-polarized electron current, that is, splitting of spin bands because of the spin magnetic moment induced. The combined effects of the tunneling barriers and SOC can be used to implement spin transistor devices^{82,83}. Various successful tight binding (TB) models implementing spin orbit (SO) interaction are presented in the literature^{29,84–86}. The SO Hamiltonian is defined as the Larmor contribution due to the spin magnetic moment⁴², and the Thomas spin precession⁸⁷,

$$H_{SO} = -\mu_S \cdot \mathbf{B} + \mathbf{\Omega}_T \cdot \mathbf{S} = \frac{e}{2m_e^2 c^2} (\nabla V \times \mathbf{p}) \cdot \mathbf{S} = \Gamma \mathbf{L} \cdot \mathbf{S}, \quad (2.59)$$

then, the electric field V of the nuclei observed by valence electrons with momentum p , e is the electron charge and c is the speed of the light. Further simplification express the SO Hamiltonian as a direct product between \mathbf{S} and \mathbf{L} corresponding to spin and orbital angular momentum operators, with a SO magnitude Γ .

Band splitting have being also attributed to asymmetry of the crystal potential, in addition to SO interaction, known as Rashba effect^{88,89}. Large Rashba splitting have been attributed to produce Fulde–Ferrell–Larkin–Ovchinnikov (FFLO) states⁹⁰, topological states⁹¹, and topological superconductors⁹². The Rashba SO interaction⁹³ can be described with the Hamiltonian,

$$H_R = \lambda_R (\boldsymbol{\sigma} \times \mathbf{p}) \cdot \hat{\mathbf{n}}, \quad (2.60)$$

as λ_R is the Rashba magnitude,

$$\lambda_R = -\frac{g_e \mu_B E_0}{2m_e c^2}, \quad (2.61)$$

where E_0 is the initial electric field magnitude, $\boldsymbol{\sigma} = [\sigma_x, \sigma_y, \sigma_z]$, $\mathbf{p} = [p_x, p_y, p_z]$ is the momentum vector, g_e is the gyro electronic constant and ν_B is the Bohr magneton. Such electric field is responsible for breaking inversion symmetry in the system, known as Stark effect, and can be written as,

$$H_S = -\mathbf{E} \cdot \hat{\mathbf{n}}, \quad (2.62)$$

where $\hat{\mathbf{n}}$ is the direction of the electron spin. The Stark effect is a well-known source of symmetry breaking in spectral lines of atomic systems⁹⁴, as an analog to the Zeeman effect^{95,96}.

2.3.3 Derivation of the band folding method

LCAO allows us to define locally the wavefunctions of each atomic species. However, such components can only be expressed in large matrices that scale with the system size, making it difficult to work with analytically.

For a set of basis functions describing the electronic structure of a physical model of several particles can be a highly complex problem to solve analytically. However, such a problem can be solved by considering particular eigenstates spaces, that is, choosing Hilbert sub-spaces that contain most of the dynamics of the total Hilbert space^{80,97,98}. This method is called the Energy-independent partitioning or Band Folding method²⁹.

Let us first consider a Hamiltonian with two kinds of eigenstates α and β , and we assume they are weakly coupled to each other. The secular equation, in matrix form, can be written as,

$$\begin{pmatrix} H_{\alpha\alpha} & H_{\alpha\beta} \\ H_{\alpha\beta}^\dagger & H_{\beta\beta} \end{pmatrix} \begin{pmatrix} v_\alpha \\ v_\beta \end{pmatrix} = E \begin{pmatrix} v_\alpha \\ v_\beta \end{pmatrix}, \quad (2.63)$$

here, $H_{\alpha\alpha}$ and $H_{\beta\beta}$ are the corresponding Hamiltonian of each kind of eigenstates v_α and v_β , and $H_{\alpha\beta}$, $H_{\beta\alpha}$ are their coupling. The objective is to block diagonalize the Hamiltonian into space α by finding the unitary transformation that reduces it. Now, by solving for the eigenvalues, it is trivial to notice that

$$v_\beta = (\mathbf{1}E - H_{\beta\beta})^{-1} H_{\alpha\beta}^\dagger v_\alpha.$$

Then, solving (2.63) for v_α ,

$$\left(H_{\alpha\alpha} + H_{\alpha\beta} (\mathbf{1}E - H_{\beta\beta})^{-1} H_{\alpha\beta}^\dagger \right) v_\alpha = E v_\alpha. \quad (2.64)$$

Now, Expanding $(\mathbf{1}E - H_{\beta\beta})^{-1}$ to first order in $\frac{H_{\beta\beta}}{E}$, we find that,

$$\left(H_{\alpha\alpha} - H_{\alpha\beta} H_{\beta\beta}^{-1} H_{\alpha\beta}^\dagger \right) v_\alpha = S E v_\alpha, \quad (2.65)$$

here, $S = \left(1 + H_{\alpha\beta} (H_{\beta\beta}^{-1})^2 H_{\alpha\beta}^\dagger \right)$ is a canonical transformation in the total Hilbert Space that allow us to energy independent partitioning. Finally, the effective Hamiltonian can be found as

$$S^{-1/2} \left(H_{\alpha\alpha} - H_{\alpha\beta} (H_{\beta\beta})^{-1} H_{\alpha\beta}^\dagger \right) S^{-1/2} \Phi = E \Phi, \quad (2.66)$$

where $\Phi = S^{1/2} v_\alpha$. The physical systems based on effective interactions usually are useful to understand the main physical properties. The energy-independent effective Hamiltonian computed by Band Folding method is particular simple to obtain to first order and higher odd order⁹⁹. This approach results in a controllable perturbation theory, capable to described pretty accurate low dimensional systems e.g.measurement of spin orbit splitting in graphene and proximity effects¹⁰⁰.

2.4 Non-equilibrium Green's function calculations using density functional theory

Electronic transport (ET) calculations are important methods for understanding the chemical bond dynamics of new molecules and materials¹⁰¹, responsible for the fundamental chemical process behind any redox reaction. The first experimental realizations of molecular ET were reported in the early 2000s, where it was measured in molecular wire

junctions^{102,103}. The development of reliable theoretical methods for simulating ET through nano-scale junctions became a priority because of both general scientific interest and the introduction of a new generation of molecular-based electronics. DFT provides a convenient framework to develop reliable *ab initio* models for a wide range of systems, i.e., without considering system-dependent parameters. However, most methods implemented in first-principle calculations need to be restricted to either finite or periodic systems in equilibrium. Additionally, there is no rigorous theory able to use a more appropriate functional¹⁰⁴. In a real situation, a finite voltage bias is applied to the electrons in the junction, which are then driven through the junction. This is a highly -elastic scattering through a non-equilibrium system.

The Landauer^{105,106} and Büttiker¹⁰⁷ formulation for describing the current through a finite disordered region of non-interacting electrons forms the foundation of electronic transport calculations. At the nano-scale, the Landauer-Büttiker conductance can be evaluated by employing a combination of the non-equilibrium Green's function (NEGF) method and ground-state DFT. In this section, we will be describing this method.

2.4.1 Non-equilibrium electronic transport in a contact-electrode system

In the low temperature ($T \rightarrow 0$) and zero bias ($\epsilon = \epsilon_F$) limit, the linear response conductance of non-interacting electrons going through a central region (C) connected by two ballistic leads or electrodes (L, R) is defined as,

$$G = G_0 T(\epsilon_F), \quad (2.67)$$

where $T(\epsilon)$ is the elastic transport function, ϵ_F is the Fermi energy, and $G_0 = 2e^2/h = 1/\pi$ is the conductance quantum. The elastic transport function describes the probability that an electron at a given eigenenergy ϵ_i is transmitted through the junction. The retarded, \mathcal{G}^r , and advanced, \mathcal{G}^a , Green's function (GF) are defined in terms of the basis set $\{\phi_i\}$ chosen and the current, and may be expressed in term of the left and right leads and the central region as,

$$(z^r \mathcal{S} - \mathcal{H}) \mathcal{G}^r = \mathbf{1}, \quad (2.68)$$

where $z^r = \epsilon + i0^+$ is the pole of the retarded GF \mathcal{G}^r , \mathcal{H} is the Hamiltonian matrix, \mathcal{S} is the coupling matrix and $\mathbf{1}$ is the identity matrix. The advanced GF is then simply the complex conjugate transform of the retarded GF, so that $\mathcal{G}^a = (\mathcal{G}^r)^\dagger$. This equation describes the system as one of non-interacting electrons moving phase-coherently through a central conductor region from a left to right leads. Meir and Wingreen¹⁰⁸ derived a useful formula for the transmission function using NEGF in term of the regions $L - C - R$,

$$T(\epsilon) = \text{Tr} \left[\mathcal{G}_C^r(\epsilon) \Sigma_L(\epsilon) \mathcal{G}_C^a(\epsilon) \Sigma_R(\epsilon) \right] \quad (2.69)$$

where $\mathcal{G}_C^r(\epsilon)$ ($\mathcal{G}_C^a(\epsilon)$) correspond to the retarded (advanced) GF of the central (C) region basis,

$$\mathcal{G}_C^r(\epsilon) = [z^r \mathcal{S}_C - \mathcal{H}_C - \Sigma_L(z^r) - \Sigma_R(z^r)]^{-1}. \quad (2.70)$$

The lead self-energies $\Sigma_{L/R}$ for the left L or right R leads in (2.69) are defined as,

$$\Sigma_{L/R}(z) = (z \mathcal{S}_{C,L/R} - \mathcal{V}_{C,L/R}) \mathcal{G}_{L/R}^0 (z \mathcal{S}_{C,L/R}^\dagger - \mathcal{V}_{C,L/R}^\dagger) \quad (2.71)$$

where $\mathcal{V}_{C,L/R}$ and $\mathcal{S}_{C,L/R}$ are the coupling and overlap matrices between the central region atoms and the L/R lead, respectively, $\mathcal{G}_{L/R}^0 = [z\mathcal{S}_{L/R} - \mathcal{H}_{L/R}]^{-1}$ is the surface GF describing the semi-infinite L/R lead in terms of the Hamiltonian and overlap of the same lead, which is calculated using a decimation technique¹⁰⁹. The self energy is calculated similarly using a Dyson equation¹¹⁰, where the GF connects the infinite sum of Feymann diagrams of the scattering between left (L) and right (R) leads across the central (C) region. Finally,

$$\Gamma_{L/R} = i(\Sigma_{L/R} - \Sigma_{L/R}^\dagger) \quad (2.72)$$

are the off-diagonal self energies or spectral broadening matrices for each lead region¹¹¹.

2.4.2 Non-equilibrium Green's function implementation

A convenient method for using NEGF for transport calculations has been implemented by Brandbyge *et al.*^{82,112}, as described in Fig. 2.3. By considering the same three regions, $L - C - R$, the density, overlaps and Hamiltonian matrix of each region may be expressed as a full Hamiltonian:

$$H = \begin{pmatrix} \ddots & \mathcal{V}_L & 0 & 0 & 0 \\ \mathcal{V}_L^\dagger & \mathcal{H}_L & \mathcal{V}_L & 0 & 0 \\ 0 & \mathcal{V}_L^\dagger & \mathcal{H}_C & \mathcal{V}_R & 0 \\ 0 & 0 & \mathcal{V}_R^\dagger & \mathcal{H}_R & \mathcal{V}_R \\ 0 & 0 & 0 & \mathcal{V}_R^\dagger & \ddots \end{pmatrix} \quad (2.73)$$

where \mathcal{H}_L , \mathcal{H}_R , \mathcal{H}_C are the Hamiltonian onsite matrices of the L , R and C region, respectively, and \mathcal{V}_L , \mathcal{V}_R are the coupling matrices between the L/R lead and the C region. Notice that the interaction between leads in the region of interest is set to zero since they are assumed to be negligible as there should be no interaction between non-neighboring principal layers (PLs) of the leads. Also, the leads are assuming to be semi-infinite bulk along the direction of transmission measured and electronic polarization.

The GPAW and atomic simulation environment (ASE) implement the concept of inverting the total Hamiltonian in (2.73) as a semi-infinite matrix to obtain the GF^{71,113,114} with the following considerations. As shown in Fig. 2.3, leads should include at least two PLs of metallic atoms. This means the h_1 and h_2 matrices ($\mathcal{H}_{L/R}$) should contain at least two PL, and one must be a periodic part of the Hamiltonian such that there is only coupling between nearest-neighbor PLs. To ensure we have proper interactions between the central (C) region and the electrodes or leads, h (\mathcal{H}_C) should include at least one PL where it couples to the L/R leads. Additionally, when non-orthogonal basis sets, such as those employed in LCAO, form the h , h_1 and h_2 matrices, the coupling matrices s , s_1 and s_2 should be provided. An important consideration is to ensure the system is isolated and sufficiently large that the screening takes place inside the $L - C - R$ regions due to the electrostatic potential. By using a LCAO basis in our DFT calculations, the GPAW package can directly provide the complete LCAO Hamiltonian of the entire system within the unit cell, which is necessary for performing NEGF calculations. Further details of this implementation are provided in Refs. 113 and 71.

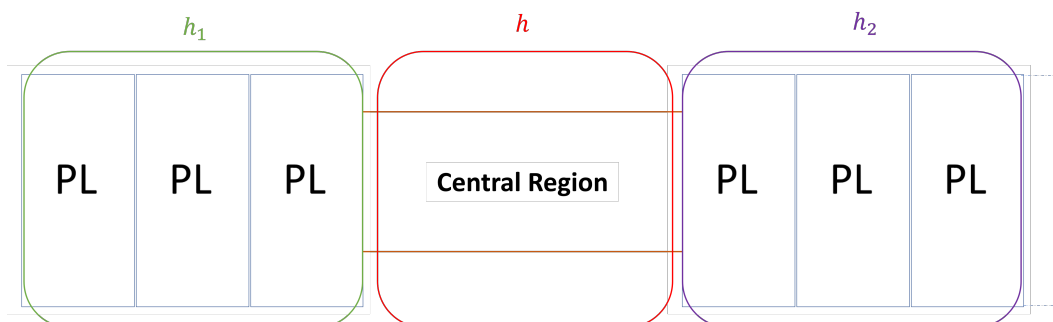


Figure 2.3: The scattering region or junction is composed of left (L) and right (R) electrode leads and a central (C) region, with Hamiltonians h_1 , h_2 , and h , respectively. Each junction includes at least two PL which only couple between neighbors. In our DFT calculations we included only one PL in the left lead, manually adding a second PL to h_1 as described in Appendix D.1. The central region includes the molecule with linker group at its ends ensuring its stability on the electrodes.

Within the DFT framework, transmission eigenchannels give a spatial understanding of the pathway of the tunneling electron in the form of a decaying wavefunction. They are the closest trajectory representation to the eigenstate responsible for carrying the electronic current. The shape of the eigenchannels is highly energy-dependent, with each one generally taking the form of the energetically nearest molecular orbitals. It is also affected by how well the molecule can transfer an electron, e.g., the wave function decays between atoms and molecules, the chemical potential, and the hopping strength. To some extent, the magnitude of each orbital's contribution can be directly related to the product of the orbital coefficients on the terminal atoms and inversely proportional to the energetic separation between the orbital and the Fermi energy, ϵ_F ^{115,116}. The eigenchannels provide a means for visually differentiating between σ and π molecular bonding and anti-bonding orbitals, which are essential for ET. However, for saturated systems, chemical bonding frameworks may not be reflected in the eigenchannels¹¹⁶. The validity of the NEGF method for modeling ET through molecular junctions based on the DFT Hamiltonian is highly dependent on both the xc functional used and the molecule in the central region itself. More computational demanding calculations for ET have been proposed within the quasiparticle GW framework, time-dependent density functional theory (TDDFT), and semi-empirical methods such as the Kubo formula. However, these methods are currently impractical computationally when compared to NEGF-DFT¹¹⁷⁻¹²⁰. A more complete benchmarking overview of NEGF-DFT using LCAO is provided in Ref. 111

2.5 Oligopeptide

An oligopeptide is defined as a short-chain peptide, that is, a polymer of amino acids (AAs) connected by an amide

group or linkages. Generally, the term is used to describe a peptide of less than 20 to 25 AA residues¹²¹.

AAs are organic molecules that contain carboxyl ($-\text{COOH}$) and amino ($-\text{NH}_2$) chemical groups, along with a side chain or residue ($-R$). Depending on the composition of $-R$, there exist about 500 different kinds of AAs. Further classifications, such as the core structural-functional group's locations as α , β , γ , or δ , are fundamental for determining their chemical reactivity¹²².

Ala is an α -AA, as shown schematically in Fig. 2.4. More specifically, ala contains a methyl ($-\text{CH}_3$) group side chain as $-R$ and is classified as a non-polar and aliphatic AA¹²³.

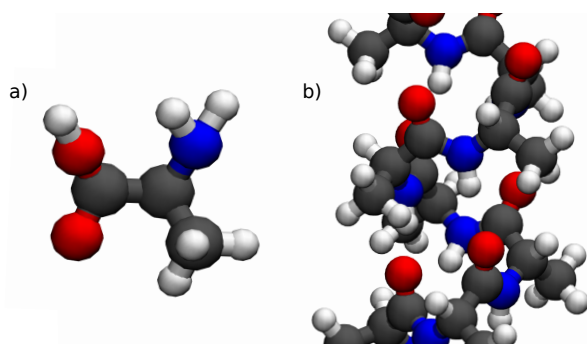


Figure 2.4: Structural schematics of (a) ala and (b) right-handed α -HAO in vacuum. C, N, O, and H atoms are depicted as grey, blue, red, and white balls, respectively.

Chapter 3

Methodology

3.1 Tight binding model for a chiral molecule

Let's consider a helical molecule shown at Fig. 4.1. Each orbital site i is distributed along the y -axis, such that $i = 1, \dots, N$. The position vector \mathbf{R}_i in the fixed or global coordinate system (xyz) is described on a cylinder with helix radii r as,

$$\mathbf{R}_i = r \cos[(i-1)\Delta\varphi] \mathbf{e}_z + r \sin[(i-1)\Delta\varphi] \mathbf{e}_x + h \frac{(i-1)\Delta\varphi}{2\pi} \mathbf{e}_y, \quad (3.1)$$

where \mathbf{e}_n are the unitary direction vector in the designated direction and h is the difference in y between turns, and $\Delta\varphi$ represents the angle between the positions of two consecutive sites. The vector that connects two sites i and j of the helix is $\mathbf{R}_{ji} = \mathbf{R}_j - \mathbf{R}_i$.

Each peptide is described with the basis set $[s, p_x, p_y, p_z]$ orbitals as $|l, m_l\rangle$, associated to the valence electrons in C, N and O as,

$$|s\rangle = |0, 0\rangle \quad |p_x\rangle = -\frac{1}{\sqrt{2}}(|1, 1\rangle - |1, -1\rangle), \quad |p_y\rangle = \frac{i}{\sqrt{2}}(|1, 1\rangle + |1, -1\rangle), \quad |p_z\rangle = \frac{1}{\sqrt{2}}|1, 0\rangle, \quad (3.2)$$

then the only p-like orbitals are assumed to have an SO matrix elements²⁹, where $z_p = \Gamma/2$ is the magnitude of

Table 3.1: SO matrix elements between p orbitals in the local coordinate system.

	$ p_x\rangle$	$ p_y\rangle$	$ p_z\rangle$
$\langle p_x $	0	$-iz_p\sigma_z^\varphi$	$iz_p\sigma_y^\varphi$
$\langle p_y $	$iz_p\sigma_z^\varphi$	0	$-iz_p\sigma_x^\varphi$
$\langle p_z $	$-iz_p\sigma_y^\varphi$	$iz_p\sigma_x^\varphi$	0

the SO interaction for p orbitals and s_j are the Pauli matrix i components in the rotating coordinate system. These

rotated spin operators are defined as,

$$\begin{aligned}\sigma_x^\varphi &= -\sin(\varphi_i)\sigma_x + \cos(\varphi_i)\sigma_z, \\ \sigma_y^\varphi &= \sigma_y, \\ \sigma_z^\varphi &= \cos(\varphi_i)\sigma_x + \sin(\varphi_i)\sigma_z.\end{aligned}\tag{3.3}$$

where φ is the rotation angle. There are two relevant SO interactions involve in the system, both spin active processes: intrinsic SO interaction due to induced magnetic fields by the overlapped p orbitals. This spin activity produces ET between π -like orbitals, with intermediate steps in the σ like orbitals. Spin transfer in first order of SO coupling, can be express as,

$$p_z^I \rightarrow E_{zx}^{IJ} \rightarrow p_x^J \rightarrow z_p \rightarrow p_z^J,\tag{3.4}$$

$$p_z^I \rightarrow E_{zy}^{IJ} \rightarrow p_y^J \rightarrow z_p \rightarrow p_z^J,\tag{3.5}$$

here, SK overlap $E_{\mu\mu'}^{IJ}$ computations are detailed in appendix C.

The second type of SO interaction considered in this model is originated as a result of a combined effect of an effective electric field generated from the hydrogen bonds. Such effect is attributed to be Stark interaction, as the main electric field generated the outside of the vicinity of the nuclei¹²⁴.

In a helical molecule, the hydrogen bond has an important role in the stabilization of the structure of helical molecules and high polarization¹²⁵. In our model, the hydrogen bond can couple s and p orbitals in the direction of the dipole field as,

$$H_K = -e\mathbf{E} \cdot \mathbf{r},\tag{3.6}$$

where \mathbf{E} is the electric field (see Ref.[126]), $\mathbf{r} = r(\sin \theta \sin \varphi, \cos \theta, \sin \theta \cos \varphi)$ is the position vector in spherical coordinates, θ being the angle with Y -axis, and e is the electron charge. In the case of local coordinates, we define the Stark contribution as,

$$H_S = -er(E_x \sin \theta \cos \varphi + E_y \cos \theta),\tag{3.7}$$

where $E_{x,y}$ are the electric field components in the x,y directions (red arrows in Fig.4.1), where the electric field source is local dipole field of hydrogen bonding.

The combined effects of Stark and SO coupling produce Rashba SO process, described by the following ET channels,

$$p_z^I \rightarrow E_{zs}^{IJ} \rightarrow p_s^J \rightarrow \xi_{sx} \rightarrow p_x^J \rightarrow z_p \rightarrow p_z^J,\tag{3.8}$$

$$p_z^I \rightarrow E_{zs}^{IJ} \rightarrow p_s^J \rightarrow \xi_{sy} \rightarrow p_y^J \rightarrow z_p \rightarrow p_z^J.\tag{3.9}$$

The ET paths of (3.4), 3.5 3.8 and 3.9 can be visualized as combination of hopping processes in Fig 4.1. Now, we can construct an effective Hamiltonian according to Ref.^{23,29}, when the π -Hamiltonian can be treated as our main effective Hamiltonian, and σ -Hamiltonian as perturbation. First, we establish the Hamiltonian in the chosen basis set of atomic orbitals,

$$H = \begin{pmatrix} H_{\pi\pi} & T \\ T^\dagger & H_{\sigma\sigma} \end{pmatrix},\tag{3.10}$$

here, H_π and H_σ are the structural Hamiltonians and T correspond to the connection between π and σ Hilbert spaces.

3.2 Spin-polarized calculations with linear combination of atomic orbitals basis sets

The spin-polarized DFT calculation of α -HAO was performed using the GPAW package⁷¹ as described in Sec. 2.1.7. We employed the PBE xc functional, a GGA developed by Perdew, Burke, and Ernzerhof⁶¹. To represent the KS wavefunctions, we employ a LCAO DZP basis set and a Γ -point sampling of the IBZ for a large lattice. Structural relaxation was performed until the maximum force on the nuclei, $F_{\max} = \max_j |\mathbf{F}_j|$ was less than 0.05 eV/Å to obtain the ground state of the oligopeptide. The oligopeptide was relaxed in gas phase employing non-periodic boundary conditions (PBC), i.e., requiring the KS wavefunctions φ_i and electron density ρ to be zero at the unit cell boundary, with 5 Å of vacuum in the x , y , and z directions.

Due to the incommensurability in the axial or helix direction of this chiral molecule, a fully periodical cell was not be found. However, a qualitative study of the tunneling and hopping mechanism of ET with this limitation may be performed, by relaxing both a two-turn and three-turn oligopeptide. The main advantage of this type of study, is the possibility of calculating qualitatively the metallic behaviour of the chiral molecule, the spin up (\uparrow) and down (\downarrow) splitting, and the ET dynamics and their dependence on the oligopeptide's length.

3.3 Electronic transport calculations in the atomic simulation environment

The central (C) region consists of two turns of α -HAO and two PLs, one adjacent to each electrode. Each PL consists of three Au(111) 5×6 layers, or 90 Au atoms, as shown in Fig. 3.1. As discussed in Sec. 2.4, this ensures that the

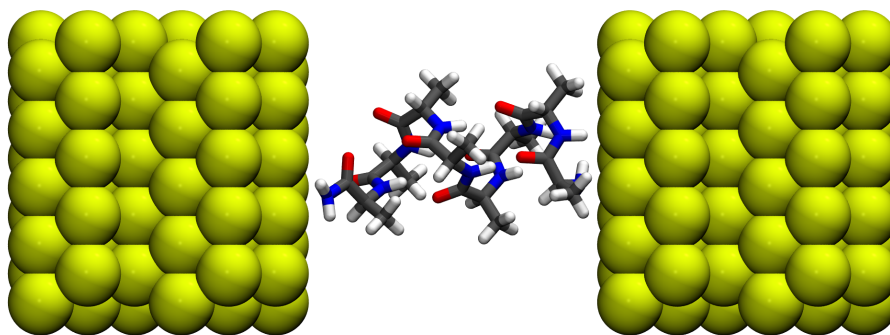


Figure 3.1: Schematic representation of the scattering region with Au(111) six layer 5×6 surface slabs as electrodes of 180 atoms on side and the two turn α -HAO chiral molecule and $-\text{NH}_2$ linker groups with chemical formula $\text{C}_{24}\text{N}_9\text{O}_8\text{H}_{43}$ forming the junction. C, N, O and H atoms are shown in grey, blue, red, and white, respectively.

overlaps between electrodes are zero. The central region is connected with the electrodes by $-\text{NH}_2$ linker groups to obtain chemical stability¹²⁷.

NEGF-DFT calculations have proven to be effective at measuring ET as described in Sec. 2.4. This method has already produced several theoretical studies of 1D electrode–molecular–electrode junction devices^{128–130}. To simulate the experimental setup, two physical electrodes were attached at each end to the two-turn ala oligopeptide in order to simulate a table-top ET experiment^{26 19,131 132}.

Since Au (111) is a diamagnetic surface, these calculations will explore the role of the chiral molecule alone as a spin filter¹⁸ as shown in Fig. 3.1.

We performed a structural relaxation of the junction using the GPAW and ASE software packages for the scattering region in the framework of DFT until $F_{\text{max}} \leq 0.05 \text{ eV}/\text{\AA}$ was obtained. In this way we ensure the structural stability of the junction and avoid obtaining nonphysical ET spectra. We used PBE as the xc functional, performed spin-polarized calculations and employed scalar-relativistic pseudopotentials within the PAW methodology. The scattering region was relaxed with PBCs in all directions. The LCAO atomic basis sets were chosen to provide a realistic description of experimental conditions with a defined number of spherical harmonics¹³³. Specifically, we employed the basis sets for each species as shown in Table 3.2.

Table 3.2: LCAO basis set and number of basis functions employed for each atomic species.

Atom	Basis Set	# of Basis Functions
C	DZP	13
O	DZP	13
H	DZP	5
N	DZP	13
Au	SZP	9

We employed a dense grid spacing of $h \approx 0.1 \text{ \AA}$ to provide an improved description of the ground state density, forces, and wave functions. For a realistic description of the electronic occupations, we employed a room temperature ($k_B T \approx 25 \text{ meV}$) Fermi–Dirac smearing, which still produced fractional occupations near the Fermi level.

For the structural relaxation of the scattering region the leads are “frozen”, i.e., the positions of the Au nuclei \mathbf{R}_I are fixed and the oligopeptide is allowed to relax. We also studied the compression effect in the energy difference of the HOMO and LUMO.

Chapter 4

Results & Discussion

4.1 Derivation of effective Hamiltonian

4.1.1 The effective model

Let us consider an ideal helix as shown in Figure Fig. 4.1¹, as we discuss in Methodology(see Sec. 3.1). The conduction electron is assumed to be provided by the $-\text{COOH}$ group¹³⁴ attached by hydrogen bonding to the NH_2 group (or site). The high polarization of the hydrogen bond induces a local electric field along the helical molecule. The hydrogen is not parallel to the y axis, since in the real structure there is a small tilt⁴ that we captured in our model. The backbone of the oligopeptide is conformed by σ bonding, i.e. s, p_x, p_y , that line tangential to the oligopeptide shape. Meanwhile, p_z orbitals point in the radial direction. This arraignment led to several ET paths as described in 3.1. A important consideration is that ET between p_z orbitals is small compared to the direct $p_z - p_z$ kinetic contribution, such that they omitted in our model.

The full Hamiltonian of our model can be written as,

$$H = H_K + H_{SO} + H_S, \quad (4.1)$$

where H_K is the Kinetic term or the SK overlaps, H_{SO} is the Spin-Orbit term and H_S is the Stark interaction term. In the Table B.1, the kinetic or LCAO overlaps are represented by V_s, V_x, V_y and V_z , later computed using Harrison Formula⁷⁰ (see Appendix A and C), site energies ϵ_p^σ and ϵ_p^π correspond to bonded orbitals $p_{x,y}$ and conduction orbitals p_z , and ϵ_s is the site energy of s orbitals. Using the BF method described in Sec. 2.3.3, the effective Hamiltonian can be described in terms of the π and σ spaces, considering the σ structure as a perturbation of the π structure²⁹. The full Hamiltonian is presented in App. B.

Now, the Full Hamiltonian can be mapped to an effective Hamiltonian by considering the π -structure Hamiltonian as the most physically meaningful and σ -structure as a perturbation. To achieve this, we employ an energy-independent perturbative approach discussed in 2.66. It is similar to the Foldy-Wouthuysen transformation¹³⁵, maintaining just the first order perturbation of the Hamiltonian. As a result, we mapped a 8×8 Hamiltonian to an

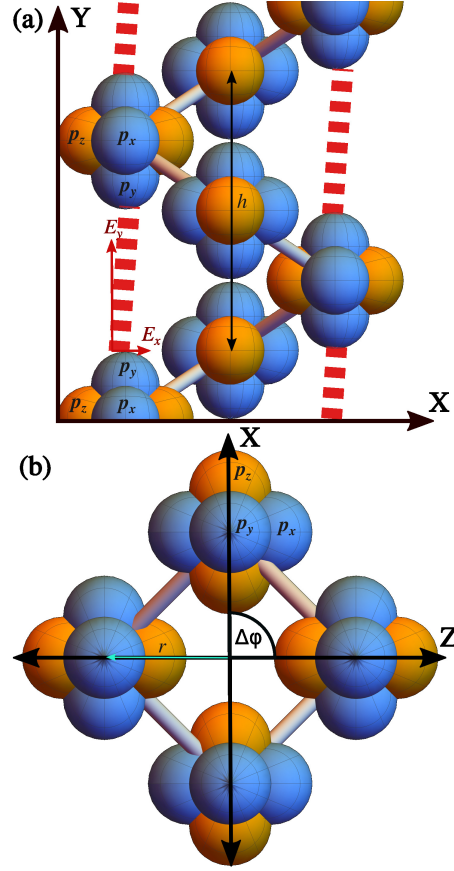


Figure 4.1: (a) Front view of the helical oligopeptide in the xy -plane. Here h is the helical pitch and each p -orbital are labelled. The internal electric field caused by the hydrogen bond high polarization and the component along each direction are shown in red. (b) Top view of the helical oligopeptide in the XZ -plane where r represents the radius of the helix, and $\Delta\varphi$ is the angle between consecutive AAAs. Extracted from Torres *et al.*¹

effective 2×2 Hamiltonian, without no additional corrections due to wavefunction normalization¹³⁶. The Hamiltonian in the basis of atomic orbitals for oligopeptide in (3.10) is,

$$\mathcal{H} \approx H_\pi - TH_\sigma^{-1}T^\dagger. \quad (4.2)$$

Then, the effective Hamiltonian for the π -structure can be written as,

$$\mathcal{H} = \begin{pmatrix} \epsilon_\pi & V_z - i((\boldsymbol{\alpha} + \boldsymbol{\lambda}) \times \mathbf{s})_z \\ V_z + i((\boldsymbol{\alpha} + \boldsymbol{\lambda}) \times \mathbf{s})_z & \epsilon_\pi \end{pmatrix}. \quad (4.3)$$

Here, the Intrinsic SO components, up to first order, are linear in z_p , and Rashba bi-linear in $z_p \epsilon_{sy}$, that contribute to the total SO interaction related to the π -structure, in concordance of path considered in (3.4), 3.5, 3.8, 3.9. Then,

there is no correction for the kinetic interaction. The intrinsic SO terms between sides i and j is given by,

$$\mathcal{H}_{so}^{xy} = i(\alpha_x \sigma_y^{\phi} - \alpha_y \sigma_x^{\phi}) = i(\boldsymbol{\alpha} \times \mathbf{s})_z, \quad (4.4)$$

here \mathbf{s} is the Pauli matrix vector and $\boldsymbol{\alpha}$ is the Intrinsic SO vector in the x, y directions,

$$\alpha_x = \frac{2z_p V_x}{\epsilon_p}, \quad \alpha_y = \frac{2z_p V_y}{\epsilon_p}. \quad (4.5)$$

Both values are considered to be characteristic to the oligopeptide, and computed as $\alpha_x \sim 8.97$ meV and $\alpha_y \sim 10.20$ meV (see appendix A.1). In the same way, the Rashba SO term have bi-linear contribution from SO and Stark interaction,

$$\mathcal{H}_R^{ij} = i(\lambda_x \sigma_y^{\phi} - \lambda_y \sigma_x^{\phi}) = i(\boldsymbol{\lambda} \times \mathbf{s})_z, \quad (4.6)$$

here $\boldsymbol{\lambda}$ is a vector with the Rashba SO magnitude in each component defined as,

$$\begin{aligned} \lambda_x &= \frac{z_p(\xi_{sy,i} - \xi_{sy,j})V_s}{\epsilon_{pz}\epsilon_s} - \frac{2z_p\epsilon_{py}^2\epsilon_s\xi_{sx}^2V_x}{\epsilon_{px}^2(\xi_{sy}^2 - \epsilon_{py}\epsilon_s)^2} \\ &+ \frac{2z_p\xi_{sx}\xi_{sy}V_y}{\epsilon_{px}(\xi_{sy}^2 - \epsilon_{py}\epsilon_s)}, \\ \lambda_y &= -\frac{2iz_p\xi_{sy}^2V_y}{\epsilon_{py}^2\epsilon_s} + \frac{2z_p\xi_{sx}\xi_{sy}V_x}{\epsilon_{px}(\xi_{sy}^2 - \epsilon_{py}\epsilon_s)}. \end{aligned} \quad (4.7)$$

The estimated values of the contributions are $\lambda_x \sim 0.15$ meV and $\lambda_y \sim 1.2$ meV (see appendix B). Note that second-order terms are included, due to smaller contribution of the first order of consecutive sites i and j , due to electric dipole difference. Since the angle of inclination of the hydrogen bond to the helix axis is small, the electric polarization ϵ_{sx} is negligible against ϵ_{sy} (see (3.7)).

The full effective SO term can be defined as $H_{SO} = H_{so} + H_R$. For later analysis, only first-order terms will be considered. However, when mechanical deformation is studied, second-order terms in Rashba components can become of comparable size to intrinsic SO components¹.

4.1.2 Bloch Space effective Hamiltonian

Consider a local Cartesian coordinate system that is on top of an atom, then each atom on the chain will have the same surrounding or system. The nearest neighbor atoms are described by the following vectors in the local system,

$$\boldsymbol{\tau}^{\pm} = \frac{r}{\sqrt{2}}(\mathbf{e}_z \pm \mathbf{e}_x) \pm \frac{h}{4}\mathbf{e}_y. \quad (4.8)$$

Only first nearest neighbors interaction are considered relevant in our model, however this can be increased to uncover new feature of chiral molecules. Then, the Hamiltonian can be expressed as the Bloch sum of matrix elements. For

an infinite long helix, $k_z = 0$, the Bloch expansion can be obtained as,

$$\begin{aligned}
\mathcal{H}(k) &= \frac{1}{N} \sum_{i=1}^N \sum_{j=1}^N e^{i\mathbf{k}\cdot\mathbf{R}_{ij}} \langle \phi_i | \mathcal{H} | \phi_j \rangle \\
&= \frac{1}{N} \sum_{i=1}^N \left(\sum_{j=i}^N \langle \phi_i | \mathcal{H} | \phi_i \rangle + \sum_{j \neq i} e^{i\mathbf{k}\cdot\mathbf{R}_{ij}} \langle \phi_i | \mathcal{H} | \phi_j \rangle \right) \\
&= \frac{1}{N} \sum_{i=1}^N (\epsilon_\pi \mathbf{1}_s + V_z f(k) \mathbf{1}_s + g(k) ((\alpha + \lambda) \times \sigma_z^\varphi) \\
&= \epsilon_\pi \mathbf{1}_s + V_z f(k) \mathbf{1}_s + g(k) ((\alpha + \lambda) \times \sigma_z^\varphi.
\end{aligned} \tag{4.9}$$

where $f(k)$ and $g(k)$ the reciprocal functions associated to diagonal spin matrix $\mathbf{1}_s$ and σ_z^φ , respectively. Notice here we have only taken nearest neighbor couplings and strict periodicity of the lattice turn by turn (our model). As shown in (4.9), ϕ_i are the orbitals per unit cell and N is the number of the unit cells in the molecule. This model considers an approximate structure, shown in Fig. 4.1, where the angle, $\Delta\phi$, between successive AAs is smaller than the angle for real oligopeptides⁴. The latter assumption is not quite correct for real oligopeptides since there is small incommensurability (non-periodicity in the axial direction) of the potential when one goes from one turn to the next, omitting a small contribution to spin polarization. However, for the sake of this study, we believe the important physical phenomena have been considered, since the Stark/Rashba contribution is not the only contributor to the spin polarization in the molecule, as we will see later.

If we consider now a local frame that satisfies $\eta = \tan(h/r)$, the effective Hamiltonian can be expressed in one dimension. Then, the primed one dimensional quantities can be defined as k , the one dimensional vector, proportional to $r' = r/\sqrt{2} + \eta h/4$, and reciprocal functions of k ,

$$f(k) = \cos(r'k), \quad g(k) = \sin(r'k). \tag{4.10}$$

The spectra of the system can be obtained by solving the secular equation

$$\det(\mathcal{H}(k) - ES) = 0, \tag{4.11}$$

where \mathbf{S} is the overlap matrix and we assume that the eigenfunctions are orthogonal, such that S is the identity matrix in $SU(2)$. By solving the full system in the previous secular equation, we obtain the spectra of the system for the two spin species, and is given by,

$$E_\pm(k) = V_z \cos(r'k) \pm |\alpha + \lambda| \sin(r'k), \tag{4.12}$$

where each band corresponds to a different spin channel.

4.1.3 Hamiltonian in vicinity of half filling

Without the lost of generality, we can consider that the electron bands are half filled when the molecule is isolated (see Fig. 4.4). By doing the system with molecular environment, such as water or any electronic donor, the polarization

of the molecule may be changed because the electron transfer (add or withdraw) from the $-\text{COOH}$ group to the environment.¹³⁷ Let us consider that the Fermi energy of p_z orbital is $\epsilon_F = 0$, just by shifting it to the origin. By solving (4.11) only for the kinetic component at half filling, $\epsilon_F = V_z \cos(k_F) = 0$, the Fermi vector is $k_F = \pi/2$. Near the Fermi level, we consider a small perturbation q around k_F , such that $k = k_F - \mathbf{q}$, and $0 < |\mathbf{q}| \ll 1$, in order to study its physics. As a result, the Bloch expansion of the system, (4.9) can be approximated as,

$$\mathcal{H}_{1/2}(q) = \epsilon_\pi + V_z q + ((\alpha + \lambda) \times \sigma_z^\varphi). \quad (4.13)$$

The spectra of the system in Fig. 4.2 shows that the bands do not cross each other, separated by a constant gap between spin up and spin down states of the order of $|\alpha| \sim 10^{-2} \text{eV}$. In such a system, the SO interaction is not coupled to momentum in the vicinity of K_\pm , due to environmental doping. Nevertheless, molecular contact with an

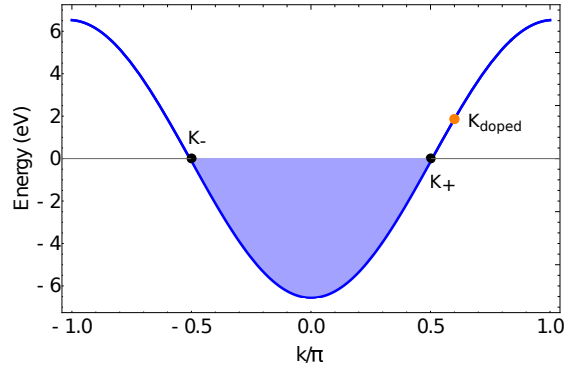


Figure 4.2: Kinetic spin degenerate bands with K_\pm points (black) and a doped point (orange) taken at $k_F = 3\pi/5$. The values for the parameters are described in Tables A.1A.2.

environment, either a surface or surrounding structure will dope the system due to the electron and charge transfer. Then, the energy must be shifted above the Fermi level $\epsilon_F = 0$. By expanding (4.3) around the doped energy k' and considering a small deviation from k_F to $k' = 3\pi/5$, we obtain,

$$\mathcal{H}_{k'}(q) = \epsilon_\pi + V_z \left(\frac{1 - \sqrt{5}}{4} - \sqrt{\frac{5 + \sqrt{5}}{8}} q \right) + ((\alpha + \lambda) \times \sigma_z^\varphi \left(\frac{1 - \sqrt{5}}{4} q + \sqrt{\frac{5 + \sqrt{5}}{8}} \right). \quad (4.14)$$

Here, the resulting Hamiltonian model a coupling between the momentum and the spin, such a correlation produces a chiral term $((\alpha + \lambda))$ that increases approaching a crossing point at $k = 0$. The previous Hamiltonian, aside from the geometrical details that determine the SO strength to within tens of meV, has the same form as that of deoxyribonucleic acid (DNA)² and Helicene¹⁴ similar theoretical models, and leads to polarized ET, as has been reported experimentally^{131,138}. Additionally, by considering the full picture as in B, or by adding more neighbors in the TB model, the SO strength can approach qualitatively to the experimental values of spin splitting, that is around 0.5 eV .

4.2 Electronic transport through α helix alanine oligopeptide

We will now explore the ET through scattering region shown in Fig. 3.1. Each electrode contributes electronic population to the system, raising the Fermi level and producing charge and electronic transfer in the density of states (DOS).

4.2.1 Length dependence of α helix alanine oligopeptide's wavefunctions

In the gas phase, the oligopeptide exhibits different near-Fermi level behavior as a function of length, as shown in Fig. 4.3. For a two turns of α -HAO, the HOMO and LUMO are clearly localized on the $-\text{NH}_2$ linker groups at the

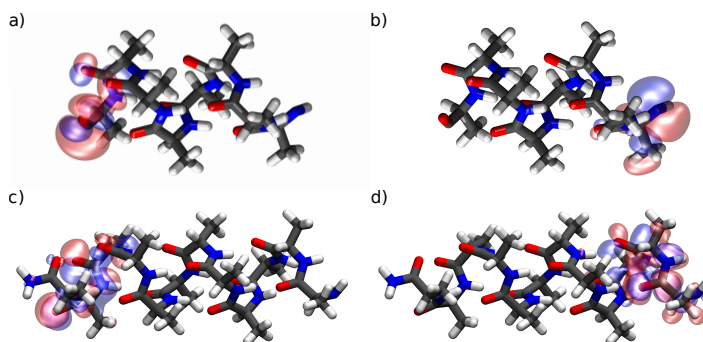


Figure 4.3: Spatial distribution of KS wavefunctions for two turns α -HAO (a) HOMO and (b) LUMO, and three turns α -HAO (c) HOMO and (d) LUMO. Positive and negative phases of the wavefunctions are in red and blue. C, N, O, and H atoms are shown in grey, blue, red, and white, respectively.

ends of the oligopeptide, with a significant p and s orbital character. When we consider a longer oligopeptide, that is, three turns of α -HAO, the spatial separation between the HOMO and LUMO is increased. When we stretched the oligopeptide in the electrode setup in the z -direction, the energy gap is reduced. We find increasing the length of the oligopeptide enhances the electronic conductance, as the electronic gap is reduced. This is consistent with previous experimental¹³¹ and theoretical studies¹. This situation may be replicated by inducing a net force, e.g., by applying a tip loading force directly in the top of the oligopeptide in a magnetic conductive atomic force microscopy (mc-AFM) setup.

For two turns of α -HAO, the HOMO and LUMO are localized mainly on the $-\text{NH}_2$ linker groups, while for three turns of α -HAO the orbitals are somewhat de-localized toward the ends of the α -HAO. This results shows the important role played by the linker group in determining the ET, as well as the length dependence.

On one hand, the radius pitch between turns in the oligopeptide is increased (decreased) when compressed (stretched), reducing (increasing) the contribution to the conductance coming from the hydrogen bonds. On the other hand, the HOMO and LUMO separation in real space (see Fig. 4.3) is reduced, adding “through space” conduction, which adds nothing to the spin-polarized conduction. As we showed in Sec 3.1, electronic hopping

dominates the spin polarization in chiral molecules with intrinsic SOC, rather than electronic tunneling, which only becomes important when the HOMO and LUMO spatial distance is short. The interplay between the preferred ET mechanism e.g. tunneling or hopping is highly tunable by stretching and may also be adjusted by adding peptides in the oligopeptide.

As a consequence, an increase in length is directly reflected in the conductance of the oligopeptide. As shown in the DOS spectra of Fig. 4.4, there is a direct dependence of the electronic gap on the length or number of turns

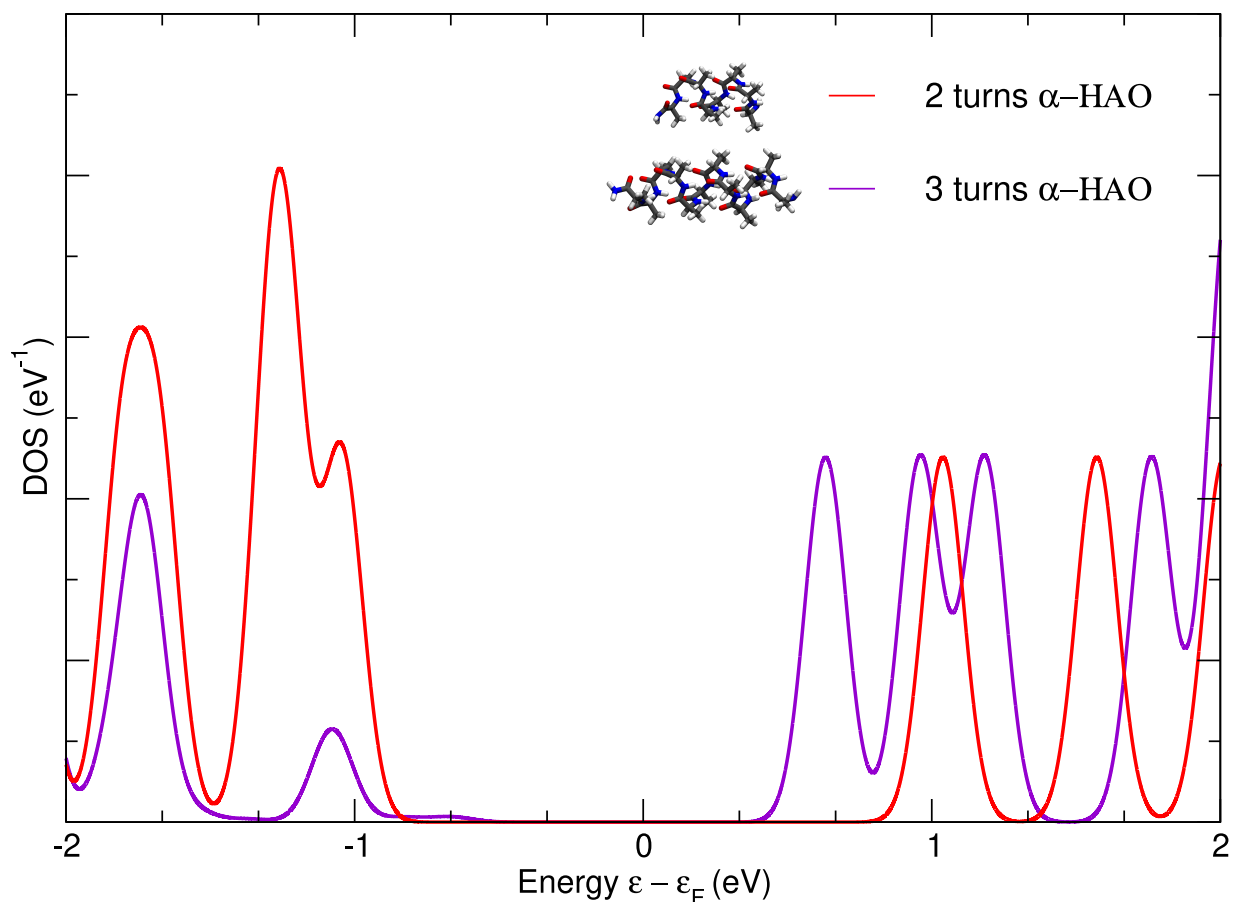


Figure 4.4: DOS of α -HAO in gas phase with two (red) and three (purple) turns as a function of energy ε in eV relative to the Fermi level ε_F .

of the oligopeptide. We find charge is transfer from the conduction bands to the valence band as we increase the molecule's length. This is consistent with experiments, where the chiral conduction related to the spin polarization, that is the spin transfer, is enhanced with the length of the chiral molecule¹³⁹.

4.2.2 Electronic transport through a α -HAO@Au slabs(111) junction

As discussed in Sec. 3.3, LCAO is used to describe the KS wavefunctions. The GPAW package⁷¹ allows one to extract the full LCAO Hamiltonian and LCAO overlaps of the system in the atomic basis. Its resulting dimension is 3178×3178 , where the first 810 atomic basis functions belong to the left (L) lead, 748 to the oligopeptide of the central (C) region, and 1620 to the right (R) lead.

The ET, as described herein, requires an equal number of PLs in the right and left lead. Due to the computational complexity and limits on available resources, computing the transmission function of the entire 3988×3988 matrix was reduced to 3178×3178 by removing one PL from one of the electrodes. For more details see Appendix D.1.

We will now consider the transmission and ET properties of the junction. As is shown in Fig. 4.5, the DOS of the junction is populated completely near the Fermi level from -1.5 to 1.5 eV. As expected, the transmission function never goes to zero in this region, just reducing its value at the point around -0.25 eV, where the DOS is zero. The transmission can be mainly attributed to the leads, since the HOMO and LUMO are mainly $5d$ orbitals of Au orbitals localized on the (111) surface. As the levels are localized at the ends of the molecule, it has phase and also with a small weight in the junction, the ET contribution is expected to be produced by tunneling. In order to further checking this hypothesis, the length of the oligopeptide should be increased, so that we may expect to observe a decrease in the raw ET from L to R Au(111) electrode.

The occupied KS wavefunctions shown in Fig. 4.6 are localized either in the oligopeptide (i), or only in one side of the molecule. In (i), the states are only present in the chiral molecule, with a little weight in the Au(111) surface and bulk. In the latter, the states are weighted in the Au(111) slabs, as well as only the left end of the molecule. As a result, the ET hopping contribution is zero in this part of the spectrum, and no tunneling is possible because of the large separation between states of the same energy. The unoccupied KS wavefunctions shown in Fig. 4.6, in contrast, are highly weighted in the Au(111) surfaces of the electrodes, with smaller contributions on the molecule at level (v) and (vi). In the latter, Rydberg states may be observed above the Au(111) surface of the gold slabs, that are also responsible for ET. Levels (v) and (vi) have significantly greater weight on the molecule connected to the right slab, also producing transport at higher energies. This is mostly due to the better absorption of the molecule on that surface. In all of these levels, the ET can be attributed to electrode–molecule–electrode hopping. We can assert that, as we increase the length of the oligopeptide, the hopping contribution should become increasingly important, as electrons travel from one site to another. The transmission function does not exhibit spin polarization, since the theoretical spin splitting may be induced by the electrode, which in this case is spin-paired²⁸.

As a consequence, the ET anisotropy is zero under these conditions, in contradiction to some experimental results. Some studies have suggested that the charge transport barrier between the two spin channels is on the order of 0.5 eV¹³². Many reasons may be provided to explain these results. These include the shape of the initial molecule, the short length of the oligopeptide used in this study, and the $-\text{NH}_2$ linker groups between the molecule and the slabs. Since scalar relativistic effective pseudopotentials have been used in our DFT framework, the SO effect may be insufficient to be observed in the molecule. Finally, these differences are perhaps due to the noble metal electrodes employed herein, whereas an Au/Ni alloy was employed experimentally¹⁴⁰.

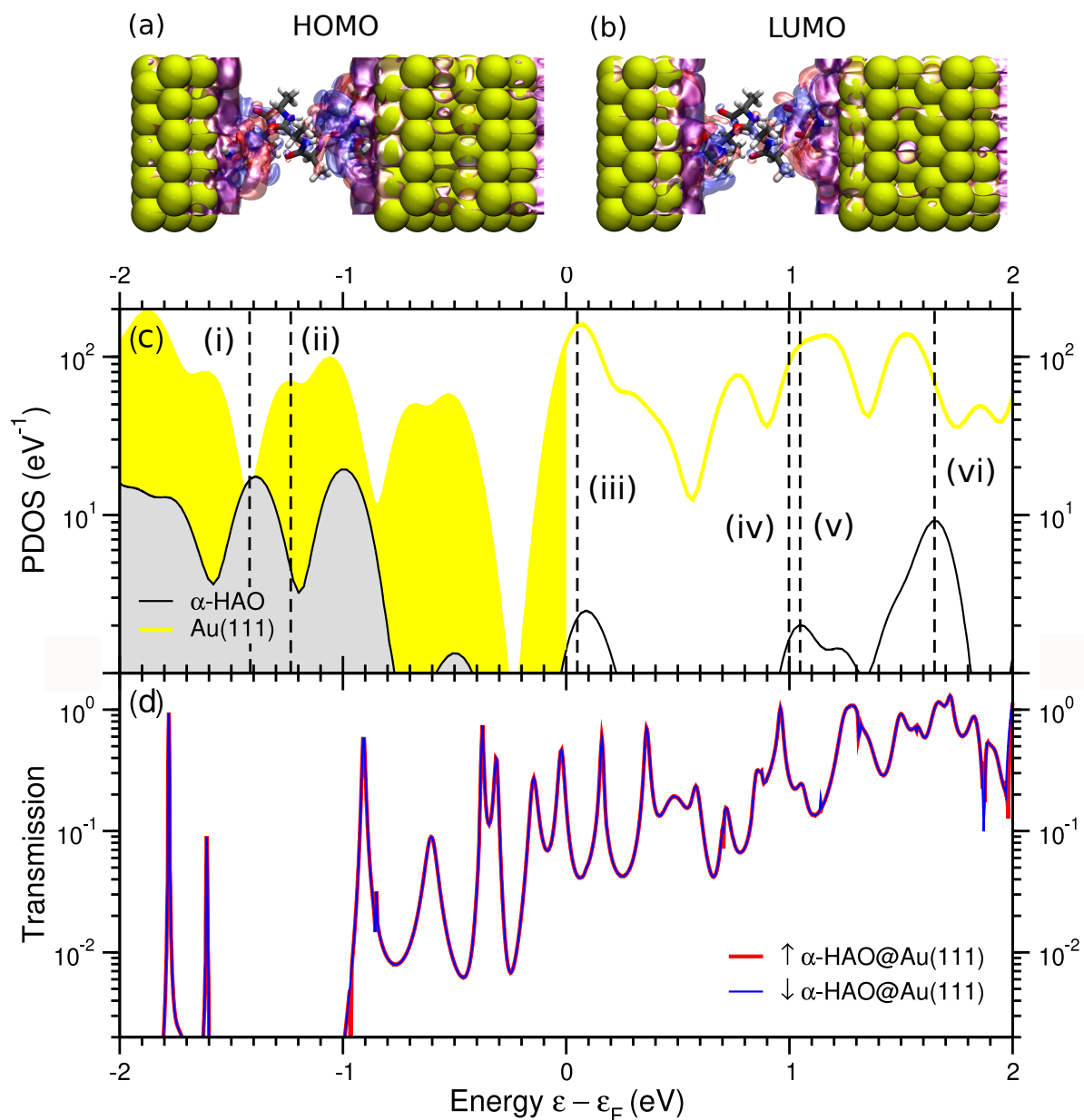


Figure 4.5: (a) HOMO and (b) LUMO pinned to the Fermi level ε_F of the α -HAO@Au(111) junction. Positive and negative isosurfaces are shown in red and blue, respectively. (c) PDOS in eV^{-1} localized on the α -HAO molecule (black) and Au(111) surface (yellow) and (d) transmission $T(\varepsilon)$ through spin up and spin down channels through the α -HAO@Au(111) junction versus energy ε relative to the Fermi level, ε_F , in eV. The eigenenergies of (i), (ii), (iii), (iv), (v), (vi) levels shown in Fig. 4.6 are marked in (c).

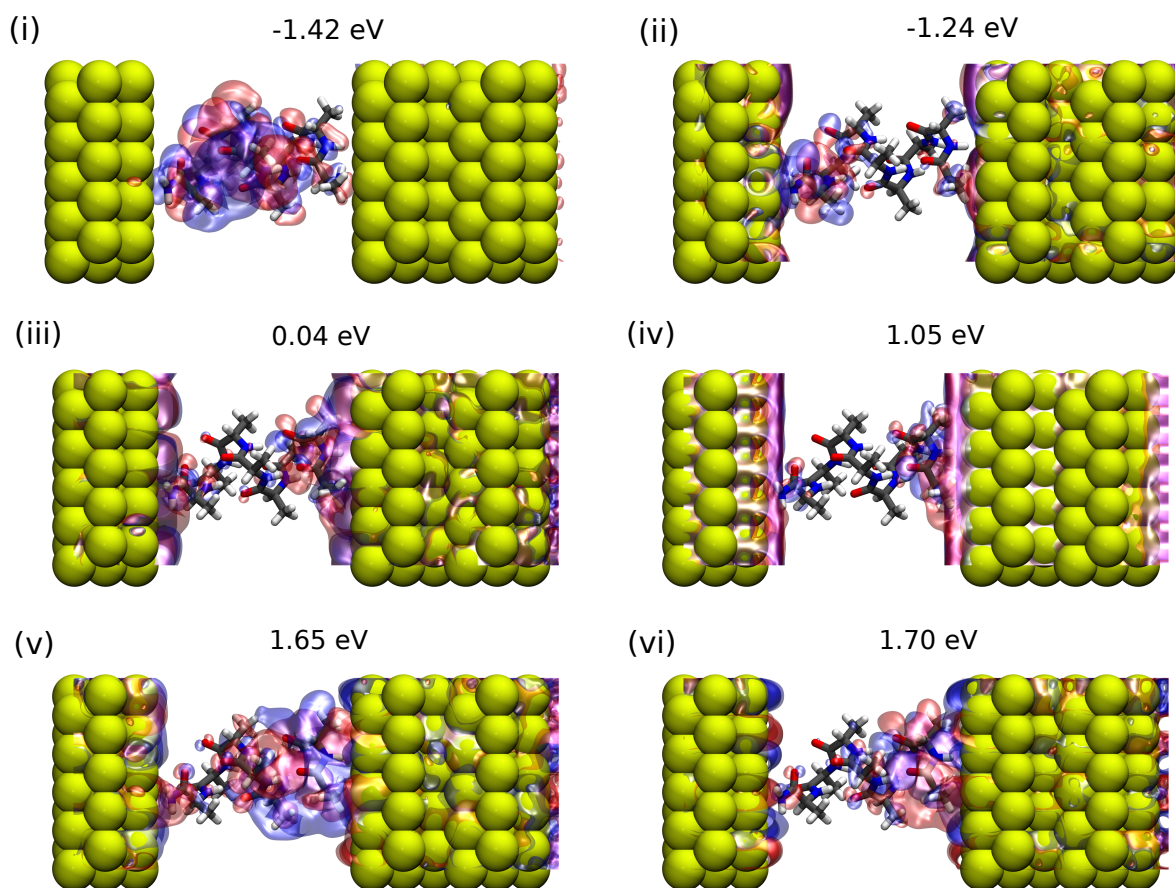


Figure 4.6: Spatial distribution of the KS wavefunctions for the α -HAO@Au(111) junction marked in Fig. 4.5(c), and their eigenenergies in eV relative to the Fermi level ε_F . Positive and negative isosurfaces are shown in red and blue, respectively.

Chapter 5

Conclusions and Outlook

In this work, we have presented a study of chiral-induced spin selectivity (CISS) dynamics of Oligopeptide molecule using DFT and TB models. We calculated the ground state wave function of α -HAO using GPAW package. It was found that the physical distance of HOMO and LUMO is proportional to the electronic band-gap, and depends on the mechanical stretching and number of peptides in the molecule, as have been shown experimentally. DOS calculation has shown that HOMO and LUMO are mostly populated by p orbitals of free electrons of N, O, and C, which is consistent with experiments.

We performed spin-polarized calculation in α -HAO@Au(111) when we obtained an metallic behaviour enhancement proportional to the oligopeptide length, in accordance to experiments. Spin filtering capabilities were not observed in the atomic levels of the isolated molecule nor the scattering region, suggesting the search of a better description of this model. Additionally, we obtained a transmission function using the NEGF method. Such transmission is attributed principally to Au d electronic states, with a significant contribution of the oligopeptide p orbitals, mainly produced by ET hopping, in the absence of spin splitting.

We proposed a TB description of the oligopeptide. By using SK overlaps, an effective Hamiltonian describing all the interactions near the Fermi level was obtained. This Hamiltonian is conformed mainly by the π structure and σ structure as a perturbation using the Down folding method. Later, we mapped this effective Hamiltonian to a half-filled Hamiltonian and showed that it can produce spin splitting because of Rashba and intrinsic SO interaction. Finally, we described the scattering problem for a similar effective Hamiltonian including Rashba SO interaction. The allowed eigenfunction inside the potential suggested spin polarization produced mainly by SO effects.

Further research can be made among this results. CISS effect may be observed in the *ab initio* context by considering a longer chiral molecules, using an appropriate linker group, or changing the structure. Since DFT is an approximated method, SO effect could not be observed precisely in the scalar-relativistic framework, requiring a fully relativistic description in the pseudopotentials used. Another possible study can be related to the choice of the metallic slab and its dependence with the transmission of the chiral molecules, since Au atoms may pair the spin state of the whole scattering region due to the proximity effects.

A three-body TB model can give rise important mechanics that can describe the SO paths to induce Spin

filtering. Also, including the higher term in the band folding expansion, may modify the effective Hamiltonian with new features, correcting the spin-polarized gap. We believe this kind of theoretical self consistent studies can give light to the spin dynamics responsible of CISS effect in chiral molecules. As promising materials for quantum computation application, the complete understanding of the ET is crucial for their future implementation.

Appendix A

Parameters for the effective Hamiltonian

We estimate the overlaps of the atomic wavefunctions using the empirical model described in ref. 70. The geometrical structure of the oligopeptide includes four atoms per turn and it does not differ significantly from realistic situations where oligopeptides are not strictly periodic from one turn to the next⁴. Atomic and structural parameters for the system are given in Table A.1. The SK and SO effective magnitudes are written in Table A.2.

Table A.1: Left column: SK parameters for s and p orbitals from². Center column: Atomic parameters for carbon atoms from^{2,3} Right column: Structural parameters used to describe the oligopeptide⁴. In realistic systems, $\Delta\phi$ is different than $\pi/2$, but this value is used to have a commensurable system.

Parameter	eV	Parameter	eV	Parameter	Å/ rad.
κ_{pp}^σ	-0.81	ϵ_p	-8.97	r	2.3
κ_{pp}^π	3.24	ϵ_s	-17.52	h	5.4
κ_{sp}	1.84	z_p	0.006	$\Delta\phi$	$\pi/2$

Table A.2: Estimation of effective interactions for the system. Left column: Hopping interactions. Right column: SO interactions.

Parameter	eV	Parameter	meV
V_s	3.786	α_x	8.97
V_x	-4.143	α_y	10.20
V_y	-7.666	λ_x	0.15
V_z	-3.265	λ_y	1.2

Appendix B

Full Hamiltonian

As covered in Sec. 2.3.1, the SK components can be computed from the atomic basis s, p_x, p_y, p_z of two sites i and j , as diagonal and off-diagonal or overlap elements.

Table B.1: The matrix elements of the full Hamiltonian in the local coordinate system corresponding to Eq 3.10. The π and σ spaces are the diagonal components while the off-diagonal correspond to T and T^\dagger of (3.10).

	$ p_z\rangle_i$	$ p_z\rangle_j$	$ s\rangle_i$	$ p_x\rangle_i$	$ p_y\rangle_i$	$ s\rangle_j$	$ p_x\rangle_j$	$ p_y\rangle_j$
$\langle p_z i$	ϵ_p^π	V_z	0	$-iz_p\mathbf{s}_y$	$iz_p\mathbf{s}_x$	V_s	V_x	V_y
$\langle p_z j$	V_z	ϵ_p^π	V_s	$-V_x$	$-V_y$	0	$-iz_p\sigma_y^\varphi$	$iz_p\sigma_x^\varphi$
$\langle s i$	0	V_s	ϵ_s	ξ_{sx}	ξ_{sy}	0	0	0
$\langle p_x i$	$iz_p\sigma_y^\varphi$	$-V_x$	ξ_{sx}	ϵ_p^σ	0	0	0	0
$\langle p_y i$	$-iz_p\sigma_x^\varphi$	$-V_y$	ξ_{sy}	0	ϵ_p^σ	0	0	0
$\langle s j$	V_s	0	0	0	0	ϵ_s	ξ_{sx}	ξ_{sy}
$\langle p_x j$	V_x	$iz_p\sigma_y^\varphi$	0	0	0	ξ_{sx}	ϵ_p^σ	0
$\langle p_y j$	V_y	$-iz_p\sigma_x^\varphi$	0	0	0	ξ_{sy}	0	ϵ_p^σ

Appendix C

Slater–Koster integrals

The overlap $E_{\mu\mu'}^{ij}$ between orbitals μ and μ' that correspond to the site i and j respectively, can be obtained using the Eq. ??^{2,14}.

The unit vector of each orbital in a local coordinate system (xyz) on-site i is given by

$$\begin{aligned}\hat{\mathbf{n}}(s_i) &= \hat{\mathbf{R}}_j, \\ \hat{\mathbf{n}}(x_i) &= -\sin(\varphi_i)\mathbf{e}_x + \cos(\varphi_i)\mathbf{e}_z, \\ \hat{\mathbf{n}}(y_i) &= \mathbf{e}_y, \\ \hat{\mathbf{n}}(z_i) &= \cos(\varphi_i)\mathbf{e}_x + \sin(\varphi_i)\mathbf{e}_z,\end{aligned}\tag{C.1}$$

The SK terms have a dependence on the distance representing in the empirical expression in the literature⁷⁰,

$$V_{\mu\mu'}^{\pi,\sigma} = k_{\mu\mu'}^{\pi,\sigma} \frac{\hbar^2}{mR_j^2},\tag{C.2}$$

where m is the mass of the electron and $k_{\mu\mu'}^{\pi,\sigma}$ depend on the specific set of orbitals or atoms.

Without loss of generality we can assume that $E_{\mu\mu'}^{ij} = 0$, where $\mu = \{s, p_x, p_y\}$, because those electrons are bonding. The SK integrals that are relevant for transport processes, in terms of general parameters of the structure,

are the following:

$$\begin{aligned}
E_{zz}^{ij} &= \langle z_i | V | z_j \rangle = \\
&\quad \cos[\Delta\varphi] V_{pp}^\pi - \frac{r^2}{|\mathbf{R}_{ji}|^2} (1 - \cos[\Delta\varphi])^2 (V_{pp}^\sigma - V_{pp}^\pi) \\
E_{zx}^{ij} &= \langle z_i | V | x_j \rangle = \\
&\quad \sin[\Delta\varphi] \left(V_{pp}^\pi - \frac{r^2}{|\mathbf{R}_{ji}|^2} (1 - \cos[\Delta\varphi]) (V_{pp}^\sigma - V_{pp}^\pi) \right) \\
E_{zy}^{ij} &= \langle z_i | V | y_j \rangle = \\
&\quad - \frac{hr}{|\mathbf{R}_{ji}|^2} (1 - \cos[\Delta\varphi]) (j - i) (V_{pp}^\sigma - V_{pp}^\pi) \\
E_{zs}^{ij} &= \langle z_i | V | s_j \rangle = \frac{r(1 - \cos[\Delta\varphi])}{|\mathbf{R}_{ji}|} V_{sp}^\sigma.
\end{aligned} \tag{C.3}$$

Using the geometry shown in Fig. 4.1, i.e. $\Delta\phi = \pi/2$, the following symmetry relations are obtained:

$$\begin{aligned}
V_z &= E_{zz}^{ij} = E_{zz}^{ji} = -\frac{r^2}{|\mathbf{R}_{ji}|^2} (V_{pp}^\sigma - V_{pp}^\pi), \\
V_s &= E_{zs}^{ij} = E_{zs}^{ji} = E_{sz}^{ij} = E_{sz}^{ji} = \frac{r}{|\mathbf{R}_{ji}|} V_{sp}^\sigma, \\
V_x &= E_{zx}^{ij} = -E_{zx}^{ji} = -E_{xz}^{ij} = E_{xz}^{ji} = V_{pp}^\pi - \frac{r^2}{|\mathbf{R}_{ji}|^2} (V_{pp}^\sigma - V_{pp}^\pi), \\
V_y &= E_{zy}^{ij} = -E_{zy}^{ji} = -E_{yz}^{ij} = E_{yz}^{ji} = -\frac{rh}{|\mathbf{R}_{ji}|^2} (V_{pp}^\sigma - V_{pp}^\pi).
\end{aligned} \tag{C.4}$$

Appendix D

Full linear combination of atomic orbitals Hamiltonian construction: overlaps and couplings

The initial LCAO Hamiltonian and the coupling matrix have 3178×3178 overlap elements. The Hamiltonian space includes two electrodes of one and two PL respectively, as well as a two-turn α -HAO molecule in the central region. The procedure described in Sec. 3.3 requires the same number of PL in the two electrodes. To achieve this requirement, we added a copy of PL to construct a Full LCAO Hamiltonian in the top left corner of the initial LCAO Hamiltonian. As Fig. D.1 include matrix elements includes a copy of the PL in the left electrode (green), intra-PL overlaps from the electrode of the right (marked in purple), and zero elements for the overlap matrix between inter-PL sites or electrodes since they are needed to not have interaction between each other. This can be achieved just by matrix manipulation. This procedure allows us to construct a Full LCAO Hamiltonian to calculate the transmission function as the literature suggests¹³³. The disadvantages of this manipulation are that the interaction of the PL added to the central region is not fully accounted for.

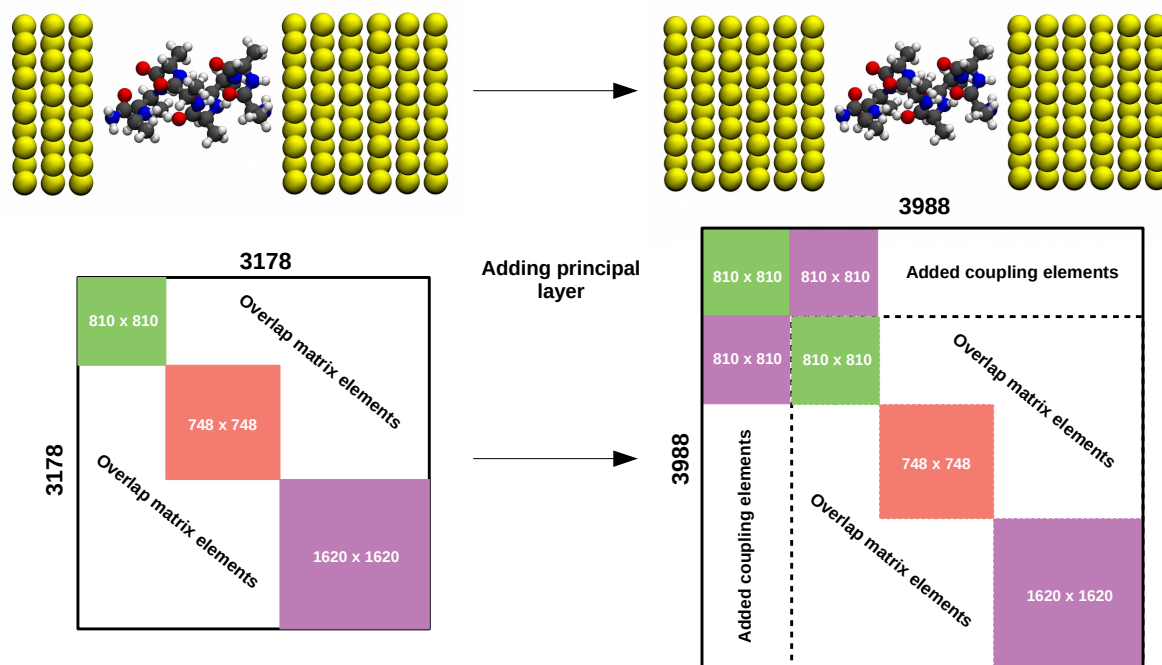


Figure D.1: To the left: Matrix distribution of LCAO components of the setup used in this study. To the right: Re-arrangement of the LCAO overlap matrices, by adding one PL to the left of the scattering region. Notice that the dimension of the LCAO Hamiltonian increase from 3178×3178 to 3988×3988 , that includes LCAO site energies and overlap terms from the added PL, to the rest of the scattering region. The purple square in the upper left corner represent the same overlap matrices between PLs as the one present in the lower right matrix elements of PLs.

Bibliography

- [1] Torres, J. D.; Hidalgo-Sacoto, R.; Varela, S.; Medina, E. Mechanically modulated spin-orbit couplings in oligopeptides. *Phys. Rev. B* **2020**, *102*, 035426.
- [2] Varela, S.; Mujica, V.; Medina, E. Effective spin-orbit couplings in an analytical tight-binding model of DNA: Spin filtering and chiral spin transport. *Phys. Rev. B* **2016**, *93*, 155436.
- [3] Konschuh, S.; Gmitra, M.; Fabian, J. Tight-binding theory of the spin-orbit coupling in graphene. *Phys. Rev. B* **2010**, *82*, 245412.
- [4] Pauling, L.; Corey, R. B.; Branson, H. R. The structure of proteins: Two hydrogen-bonded helical configurations of the polypeptide chain. *Proc. Natl. Acad. Sci. U.S.A.* **1951**, *37*, 205–211.
- [5] Quizhpi, F. M. Modelo Macro de Transferencia de Tecnología para el Ecuador. **2013**,
- [6] Gallagher, W. J.; Parkin, S. S. Development of the magnetic tunnel junction MRAM at IBM: From first junctions to a 16-Mb MRAM demonstrator chip. *IBM J. Res. Dev.* **2006**, *50*, 5–23.
- [7] Buhrman, R. Spin torque MRAM — Challenges and prospects. 2009, 33–33.
- [8] Moore, G. E. Cramming more components onto integrated circuits. *Proceedings of the IEEE* **1998**, *86*, 82–85.
- [9] Waldrop, M. M. The chips are down for Moore’s law. *Nature News* **2016**, *530*, 144.
- [10] Gibney, E. The super materials that could trump graphene. *Nature News* **2015**, *522*, 274.
- [11] Rocha, A. R.; Garcia-Suarez, V. M.; Bailey, S. W.; Lambert, C. J.; Ferrer, J.; Sanvito, S. Towards molecular spintronics. *Nature Materials* **2005**, *4*, 335–339.
- [12] Baibich, M. N.; Broto, J. M.; Fert, A.; Van Dau, F. N.; Petroff, F.; Etienne, P.; Creuzet, G.; Friederich, A.; Chazelas, J. Giant magnetoresistance of (001) Fe/(001) Cr magnetic superlattices. *Physical Review Letters* **1988**, *61*, 2472.
- [13] Molecular spintronics and quantum computing. *J. Mater. Chem.* **2009**, *19*, 1670–1671.

- [14] Geyer, M.; Gutierrez, R.; Mujica, V.; Cuniberti, G. Chirality-Induced Spin Selectivity in a Coarse-Grained Tight-Binding Model for Helicene. *J. Phys. Chem. C* **2019**, *123*, 27230.
- [15] Naaman, R.; Waldeck, D. H. Chiral-induced spin selectivity effect. *J. Phys. Chem. Lett.* **2012**, *3*, 2178–2187.
- [16] Pop, F.; Auban-Senzier, P.; Canadell, E.; Rikken, G. L.; Avarvari, N. Electrical magnetochiral anisotropy in a bulk chiral molecular conductor. *Nat. Commun.* **2014**, *5*, 1–6.
- [17] Ray, K.; Ananthavel, S.; Waldeck, D.; Naaman, R. Asymmetric scattering of polarized electrons by organized organic films of chiral molecules. *Science* **1999**, *283*, 814–816.
- [18] Göhler, B.; Hamelbeck, V.; Markus, T.; Kettner, M.; Hanne, G.; Vager, Z.; Naaman, R.; Zacharias, H. Spin selectivity in electron transmission through self-assembled monolayers of double-stranded DNA. *Science* **2011**, *331*, 894–897.
- [19] Mishra, D.; Markus, T. Z.; Naaman, R.; Kettner, M.; Göhler, B.; Zacharias, H.; Friedman, N.; Sheves, M.; Fontanesi, C. Spin-dependent electron transmission through bacteriorhodopsin embedded in purple membrane. *Proc. Natl. Acad. Sci. U.S.A.* **2013**, *110*, 14872–14876.
- [20] Guo, A.-M.; Sun, Q.-F. Spin-dependent electron transport in protein-like single-helical molecules. *Proc. Natl. Acad. Sci.* **2014**, *111*, 11658–11662.
- [21] Banerjee-Ghosh, K.; Ben Dor, O.; Tassinari, F.; Capua, E.; Yochelis, S.; Capua, A.; Yang, S.-H.; Parkin, S. S. P.; Sarkar, S.; Kronik, L.; Baczewski, L. T.; Naaman, R.; Paltiel, Y. Separation of enantiomers by their enantiospecific interaction with achiral magnetic substrates. *Science* **2018**, *360*, 1331–1334.
- [22] Yeganeh, S.; Ratner, M. A.; Medina, E.; Mujica, V. Chiral electron transport: Scattering through helical potentials. *J. Chem. Phys.* **2009**, *131*, 014707.
- [23] Medina, E.; López, F.; Ratner, M. A.; Mujica, V. Chiral molecular films as electron polarizers and polarization modulators. *EPL (Europhysics Letters)* **2012**, *99*, 17006.
- [24] Yang, X.; van der Wal, C. H.; van Wees, B. J. Spin-dependent electron transmission model for chiral molecules in mesoscopic devices. *Phys. Rev. B* **2019**, *99*, 024418.
- [25] Guo, A.-M.; Sun, Q.-f. Spin-selective transport of electrons in DNA double helix. *Phys. Rev. Lett.* **2012**, *108*, 218102.
- [26] Gutierrez, R.; Díaz, E.; Naaman, R.; Cuniberti, G. Spin-selective transport through helical molecular systems. *Phys. Rev. B* **2012**, *85*, 081404.
- [27] Gutierrez, R.; Díaz, E.; Gaul, C.; Brumme, T.; Domínguez-Adame, F.; Cuniberti, G. Modeling spin transport in helical fields: derivation of an effective low-dimensional Hamiltonian. *J. Phys. Chem. C* **2013**, *117*, 22276–22284.

- [28] Gersten, J.; Kaasbjerg, K.; Nitzan, A. Induced spin filtering in electron transmission through chiral molecular layers adsorbed on metals with strong spin-orbit coupling. *J. Chem. Phys.* **2013**, *139*, 114111.
- [29] Varela, S.; Mujica, V.; Medina, E. Effective spin-orbit couplings in an analytical tight-binding model of DNA: Spin filtering and chiral spin transport. *Phys. Rev. B* **2016**, *93*, 155436.
- [30] Varela, S.; Zambrano, I.; Berche, B.; Mujica, V.; Medina, E. Spin-orbit interaction and spin selectivity for tunneling electron transfer in DNA. *Phys. Rev. B* **2020**, *101*, 241410.
- [31] Zollner, M. S.; Varela, S.; Medina, E.; Mujica, V.; Herrmann, C. Insight into the origin of chiral-induced spin selectivity from a symmetry analysis of electronic transmission. *J. Chem. Theory Comput.* **2020**, *16*, 2914–2929.
- [32] Xie, Z.; Markus, T. Z.; Cohen, S. R.; Vager, Z.; Gutierrez, R.; Naaman, R. Spin specific electron conduction through DNA oligomers. *Nano Lett.* **2011**, *11*, 4652–4655.
- [33] Carmeli, I.; Kumar, K. S.; Heifler, O.; Carmeli, C.; Naaman, R. Spin selectivity in electron transfer in photosystem I. *Angew. Chem.* **2014**, *126*, 9099–9104.
- [34] Aragonès, A. C.; Medina, E.; Ferrer-Huerta, M.; Gimeno, N.; Teixidó, M.; Palma, J. L.; Tao, N.; Ugalde, J. M.; Giralt, E.; Díez-Pérez, I.; Mujica, V. Measuring the Spin-Polarization Power of a Single Chiral Molecule. *Small* **2017**, *13*, 1602519.
- [35] Böwering, N.; Lischke, T.; Schmidtke, B.; Müller, N.; Khalil, T.; Heinzmann, U. Asymmetry in photoelectron emission from chiral molecules induced by circularly polarized light. *Phys. Rev. Lett.* **2001**, *86*, 1187.
- [36] Kumar, A.; Capua, E.; Vankayala, K.; Fontanesi, C.; Naaman, R. Magnetless Device for Conducting Three-Dimensional Spin-Specific Electrochemistry. *Angew. Chem. Int.* **2017**, *56*, 14587–14590.
- [37] Kumar, A.; Capua, E.; Kesharwani, M. K.; Martin, J. M.; Sitbon, E.; Waldeck, D. H.; Naaman, R. Chirality-induced spin polarization places symmetry constraints on biomolecular interactions. *Proc. Natl. Acad. Sci. U.S.A.* **2017**, *114*, 2474–2478.
- [38] Mondal, P. C.; Roy, P.; Kim, D.; Fullerton, E. E.; Cohen, H.; Naaman, R. Photospintronics: magnetic field-controlled photoemission and light-controlled spin transport in hybrid chiral oligopeptide-nanoparticle structures. *Nano Lett.* **2016**, *16*, 2806–2811.
- [39] Ghosh, S.; Mishra, S.; Avigad, E.; Bloom, B. P.; Baczewski, L.; Yochelis, S.; Paltiel, Y.; Naaman, R.; Waldeck, D. H. Effect of chiral molecules on the electron's spin wavefunction at interfaces. *J. Phys. Chem. Lett.* **2020**, *11*, 1550–1557.
- [40] Born, M.; Oppenheimer, R. Zur quantentheorie der molekeln. *Annal. Ann. Phys.* **1927**, *389*, 457–484.
- [41] Ashcroft, N. W.; Mermin, N. D. *Solid State Physics*; Holt-Saunders, 1976.

- [42] Kittel, C.; McEuen, P. *Introduction to Solid State Physics*; Wiley New York, 1976; Vol. 8.
- [43] Wisesa, P.; McGill, K. A.; Mueller, T. Efficient generation of generalized Monkhorst-Pack grids through the use of informatics. *Phys. Rev. B* **2016**, *93*, 155109.
- [44] Pauli, W. Über den Zusammenhang des Abschlusses der Elektronengruppen im Atom mit der Komplexstruktur der Spektren. *Zeit. Phys.* **1925**, *31*, 765–783.
- [45] Hedin, L.; Lundqvist, B. I. Explicit local exchange-correlation potentials. *J. Phys. C* **1971**, *4*, 2064.
- [46] Haynes, P. D. Linear-scaling methods in *ab initio* quantum-mechanical calculations. Ph.D. thesis, University of Cambridge, Cambridge, 1998; Retrieved from <http://www.tcm.phy.cam.ac.uk/~pdh1001/thesis/>.
- [47] Engel, E.; Dreizler, R. M. *Density Functional Theory*; Springer, 2013.
- [48] Sholl, D.; Steckel, J. A. *Density Functional Theory: A Practical Introduction*; John Wiley & Sons, 2011.
- [49] Sham, L.; Kohn, W. One-particle properties of an inhomogeneous interacting electron gas. *Phys. Rev.* **1966**, *145*, 561.
- [50] Glanzmann, L. N. Modelling of Polymer–Carbon Nanotube Heterojunctions for Photovoltaic Applications. Ph.D. thesis, University of the Basque Country UPV/EHU, 2017.
- [51] Zeller, R. Spin-polarized DFT calculations and magnetism. *Computational Nanoscience: Do It Yourself* **2006**, *31*, 419–445.
- [52] Pant, M.; Rajagopal, A. Theory of inhomogeneous magnetic electron gas. *Solid State Commun.* **1972**, *10*, 1157–1160.
- [53] von Barth, U.; Hedin, L. A local exchange-correlation potential for the spin polarized case. i. *J. Phys. C* **1972**, *5*, 1629.
- [54] Ceperley, D. M.; Alder, B. J. Ground state of the electron gas by a stochastic method. *Phys. Rev. Lett.* **1980**, *45*, 566.
- [55] Slater, J. C. A simplification of the Hartree-Fock method. *Phys. Rev.* **1951**, *81*, 385.
- [56] Perdew, J. P.; Zunger, A. Self-interaction correction to density-functional approximations for many-electron systems. *Phys. Rev. B* **1981**, *23*, 5048.
- [57] Becke, A. D. Density-functional thermochemistry. IV. A new dynamical correlation functional and implications for exact-exchange mixing. *J. Chem. Phys.* **1996**, *104*, 1040–1046.
- [58] Gritsenko, O.; Mentel, L.; Baerends, E. On the errors of local density (LDA) and generalized gradient (GGA) approximations to the Kohn-Sham potential and orbital energies. *J. Chem. Phys.* **2016**, *144*, 204114.

- [59] Verma, P.; Truhlar, D. G. HLE16: A local Kohn–Sham gradient approximation with good performance for semiconductor band gaps and molecular excitation energies. *J. Phys. Chem. Lett.* **2017**, *8*, 380–387.
- [60] Perdew, J. P.; Burke, K.; Ernzerhof, M. Generalized Gradient Approximation Made Simple. *Phys. Rev. Lett.* **1996**, *77*, 3865–3868.
- [61] Perdew, J. P.; Burke, K.; Wang, Y. Generalized gradient approximation for the exchange–correlation hole of a many-electron system. *Phys. Rev. B* **1996**, *54*, 16533.
- [62] Zupan, A.; Burke, K.; Ernzerhof, M.; Perdew, J. P. Distributions and averages of electron density parameters: Explaining the effects of gradient corrections. *J. Chem. Phys.* **1997**, *106*, 10184–10193.
- [63] Perdew, J. P.; Ernzerhof, M.; Zupan, A.; Burke, K. Nonlocality of the density functional for exchange and correlation: Physical origins and chemical consequences. *J. Chem. Phys.* **1998**, *108*, 1522–1531.
- [64] Perdew, J. P.; Ruzsinszky, A.; Csonka, G. I.; Vydrov, O. A.; Scuseria, G. E.; Constantin, L. A.; Zhou, X.; Burke, K. Restoring the Density-Gradient Expansion for Exchange in Solids and Surfaces. *Phys. Rev. Lett.* **2008**, *100*.
- [65] Monkhorst, H. J.; Pack, J. D. Special points for Brillouin-zone integrations. *Phys. Rev. B* **1976**, *13*, 5188–5192.
- [66] Chadi, D. J.; Cohen, M. L. Special Points in the Brillouin Zone. *Phys. Rev. B* **1973**, *8*, 5747–5753.
- [67] Clark, T.; Koch, R. *The Chemist’s Electronic Book of Orbitals*; Springer, 1999; pp 5–22.
- [68] Sánchez-Portal, D.; Ordejon, P.; Artacho, E.; Soler, J. M. Density-functional method for very large systems with LCAO basis sets. *Int. J. Quantum Chem.* **1997**, *65*, 453–461.
- [69] Evarestov, R. A.; Bandura, A. V.; Losev, M.; Kotomin, E.; Zhukovskii, Y. F.; Bocharov, D. A first-principles DFT study of UN bulk and (001) surface: Comparative LCAO and PW calculations. *J. Comput. Chem.* **2008**, *29*, 2079–2087.
- [70] W.A., H. *Electronic Structure and the Properties of Solids. The Physics of the Chemical Bond*; Dover, 1989.
- [71] Enkovaara, J. *et al.* Electronic structure calculations with GPAW: A real-space implementation of the projector augmented-wave method. *J. Phys. Condens. Matter* **2010**, *22*, 253202.
- [72] Larsen, A. H. Localized Atomic Orbital Basis Sets in the Projector Augmented Wave Method. M.Sc. thesis, Technical University of Denmark, Denmark, 2008.
- [73] Sankey, O. F.; Niklewski, D. J. Ab initio multicenter tight-binding model for molecular-dynamics simulations and other applications in covalent systems. *Phys. Rev. B* **1989**, *40*, 3979.
- [74] Anglada, E.; Soler, J. M.; Junquera, J.; Artacho, E. Systematic generation of finite-range atomic basis sets for linear-scaling calculations. *Phys. Rev. B* **2002**, *66*, 205101.

- [75] Soler, J. M.; Artacho, E.; Gale, J. D.; García, A.; Junquera, J.; Ordejón, P.; Sánchez-Portal, D. The SIESTA method for ab initio order-N materials simulation. *J. Phys. Condens. Matter* **2002**, *14*, 2745.
- [76] Heine, V. *Solid State Physics*; Elsevier, 1970; Vol. 24; pp 1–36.
- [77] Heine, V.; Weaire, D. *Solid State Physics*; Elsevier, 1970; Vol. 24; pp 249–463.
- [78] Blöchl, P. E. Projector augmented-wave method. *Phys. Rev. B* **1994**, *50*, 17953.
- [79] Slater, J. C.; Koster, G. F. Simplified LCAO method for the periodic potential problem. *Phys. Rev.* **1954**, *94*, 1498.
- [80] Löwdin, P.-O. A note on the quantum-mechanical perturbation theory. *J. Chem. Phys.* **1951**, *19*, 1396–1401.
- [81] Medina, E.; González-Arraga, L. A.; Finkelstein-Shapiro, D.; Berche, B.; Mujica, V. Continuum model for chiral induced spin selectivity in helical molecules. *J. Chem. Phys.* **2015**, *142*, 194308.
- [82] Bransden, B. H.; Joachain, C. J.; Plivier, T. J. *Physics of Atoms and Molecules*; Pearson education, 2003.
- [83] Tan, S. G.; Jalil, M. B. *Introduction to the Physics of Nanoelectronics*; Elsevier, 2012.
- [84] Huertas-Hernando, D.; Guinea, F.; Brataas, A. Spin-orbit coupling in curved graphene, fullerenes, nanotubes, and nanotube caps. *Phys. Rev. B* **2006**, *74*, 155426.
- [85] Min, H.; Hill, J.; Sinitsyn, N. A.; Sahu, B.; Kleinman, L.; MacDonald, A. H. Intrinsic and Rashba spin-orbit interactions in graphene sheets. *Phys. Rev. B* **2006**, *74*, 165310.
- [86] Yao, Y.; Ye, F.; Qi, X.-L.; Zhang, S.-C.; Fang, Z. Spin-orbit gap of graphene: First-principles calculations. *Phys. Rev. B* **2007**, *75*, 041401.
- [87] Thomas, L. H. The motion of the spinning electron. *Nature* **1926**, *117*, 514–514.
- [88] Bychkov, Y. A.; Rashba, É. I. Properties of a 2D electron gas with lifted spectral degeneracy. *JETP Lett.* **1984**, *39*, 78.
- [89] Rashba, E.; Sheka, V. Symmetry of energy bands in wurzite-type crystals. II. Symmetry of bands taking into account the spin interactions. *Fiz. Tverd. Tela (Leningrad)* **1959**, *1*, 162.
- [90] Trushin, M.; Vybörnÿ, K.; Moraczewski, P.; Kovalev, A. A.; Schliemann, J.; Jungwirth, T. Anisotropic magnetoresistance of spin-orbit coupled carriers scattered from polarized magnetic impurities. *Phys. Rev. B* **2009**, *80*, 134405.
- [91] Sato, M.; Fujimoto, S. Topological phases of noncentrosymmetric superconductors: Edge states, Majorana fermions, and non-Abelian statistics. *Phys. Rev. B* **2009**, *79*, 094504.

- [92] Mourik, V.; Zuo, K.; Frolov, S. M.; Plissard, S.; Bakkers, E. P.; Kouwenhoven, L. P. Signatures of Majorana fermions in hybrid superconductor-semiconductor nanowire devices. *Science* **2012**, *336*, 1003–1007.
- [93] Griffiths, D. J. *Introduction to Electrodynamics*; American Association of Physics Teachers, 2005.
- [94] Autler, S. H.; Townes, C. H. Stark effect in rapidly varying fields. *Phys. Rev.* **1955**, *100*, 703.
- [95] Herbst, I.; Simon, B. Stark effect revisited. *Phys. Rev. Lett.* **1978**, *41*, 67.
- [96] McGurk, J.; Tigelaar, H.; Rock, S.; Norris, C.; Flygare, W. Detection, assignment of the microwave spectrum and the molecular Stark and Zeeman effects in CSe, and the Zeeman effect and sign of the dipole moment in CS. *J. Chem. Phys.* **1973**, *58*, 1420–1424.
- [97] Löwdin, P.-O. Studies in Perturbation Theory. V. Some Aspects on the Exact Self-Consistent Field Theory. *J. Math. Phys.* **1962**, *3*, 1171–1184.
- [98] Löwdin, P.-O. Studies in perturbation theory. x. lower bounds to energy eigenvalues in perturbation-theory ground state. *Phys. Rev.* **1965**, *139*, A357.
- [99] Boykin, T. B. Effective interactions and block diagonalization in quantum-mechanical problems. *J. Math. Chem.* **2014**, *52*, 1599–1609.
- [100] López, A.; Colmenárez, L.; Peralta, M.; Mireles, F.; Medina, E. Proximity-induced spin-orbit effects in graphene on Au. *Phys. Rev. B* **2019**, *99*, 085411.
- [101] Fulde, P. *Electron Correlations in Molecules and Solids*; Springer Science & Business Media, 1995; Vol. 100.
- [102] Agrait, N.; Yeyati, A. L.; Van Ruitenbeek, J. M. Quantum properties of atomic-sized conductors. *Phys. Rep.* **2003**, *377*, 81–279.
- [103] Nitzan, A.; Ratner, M. A. Electron transport in molecular wire junctions. *Science* **2003**, *300*, 1384–1389.
- [104] Kurth, S.; Perdew, J. P.; Blaha, P. Molecular and solid-state tests of density functional approximations: LSD, GGAs, and meta-GGAs. *Int. J. Quantum Chem.* **1999**, *75*, 889–909.
- [105] Landauer, R. Spatial variation of currents and fields due to localized scatterers in metallic conduction. *IBM J. Res. Dev.* **1957**, *1*, 223–231.
- [106] Landauer, R. Electrical resistance of disordered one-dimensional lattices. *Philos. Mag.* **1970**, *21*, 863–867.
- [107] Büttiker, M. Four-Terminal Phase-Coherent Conductance. *Phys. Rev. Lett.* **1986**, *57*, 1761–1764.
- [108] Meir, Y.; Wingreen, N. S. Landauer formula for the current through an interacting electron region. *Phys. Rev. Lett.* **1992**, *68*, 2512.

- [109] Guinea, F.; Tejedor, C.; Flores, F.; Louis, E. Effective two-dimensional Hamiltonian at surfaces. *Phys. Rev. B* **1983**, *28*, 4397.
- [110] Dyson, F. J. The *S* Matrix in Quantum Electrodynamics. *Phys. Rev.* **1949**, *75*, 1736–1755.
- [111] Strange, M.; Kristensen, I. S.; Thygesen, K. S.; Jacobsen, K. W. Benchmark density functional theory calculations for nanoscale conductance. *J. Chem. Phys.* **2008**, *128*, 114714.
- [112] Brandbyge, M.; Mozos, J.-L.; Ordejón, P.; Taylor, J.; Stokbro, K. Density-functional method for nonequilibrium electron transport. *Phys. Rev. B* **2002**, *65*, 165401.
- [113] Larsen, A. H. *et al.* The atomic simulation environment—a Python library for working with atoms. *J. Phys. Condens. Matter* **2017**, *29*, 273002.
- [114] Mortensen, J. J.; Hansen, L. B.; Jacobsen, K. W. Real-space grid implementation of the projector augmented wave method. *Phys. Rev. B* **2005**, *71*, 035109.
- [115] Yoshizawa, K.; Tada, T.; Staykov, A. Orbital views of the electron transport in molecular devices. *J. Am. Chem. Soc.* **2008**, *130*, 9406–9413.
- [116] Jensen, A.; Garner, M. H.; Solomon, G. C. When Current Does Not Follow Bonds: Current Density in Saturated Molecules. *J. Phys. Chem. C* **2019**, *123*, 12042–12051.
- [117] Delaney, P.; Greer, J. C. Correlated electron transport in molecular electronics. *Phys. Rev. Lett.* **2004**, *93*, 036805.
- [118] Thygesen, K. S.; Rubio, A. Conserving G W scheme for nonequilibrium quantum transport in molecular contacts. *Phys. Rev. B* **2008**, *77*, 115333.
- [119] Droghetti, A.; Rungger, I. Quantum transport simulation scheme including strong correlations and its application to organic radicals adsorbed on gold. *Phys. Rev. B* **2017**, *95*, 085131.
- [120] Varga, K. Time-dependent density functional study of transport in molecular junctions. *Phys. Rev. B* **2011**, *83*, 195130.
- [121] Lambert, J.-F. In *Encyclopedia of Astrobiology*; Gargaud, M., Amils, R., Quintanilla, J. C., Cleaves, H. J. J., Irvine, W. M., Pinti, D. L., Viso, M., Eds.; Springer Berlin Heidelberg: Berlin, Heidelberg, 2011; pp 1174–1174.
- [122] Wagner, I.; Musso, H. New Naturally Occurring Amino Acids. *Angew. Chem. Int.* **1983**, *22*, 816–828.
- [123] GDR, H. B.; Sharon, N.; Australia, E. W. Nomenclature and symbolism for amino acids and peptides. *Pure Appl. Chem.* **1984**, *56*, 595–624.
- [124] Ruiz-Blanco, Y. B.; Almeida, Y.; Sotomayor-Torres, C. M.; García, Y. *PLOS ONE* **2017**, *12*, e0185638.

- [125] Liu, C.; Ponder, J. W.; Marshall, G. R. Helix stability of oligoglycine, oligoalanine, and oligo- β -alanine dodecamers reflected by hydrogen-bond persistence. *Proteins* **2014**, *82*, 3043–3061.
- [126] Varela, S.; Mujica, V.; Medina, E. *Chimia* **2018**, *72*, 411.
- [127] Kristensen, I. S.; Mowbray, D.; Thygesen, K. S.; Jacobsen, K. W. Comparative study of anchoring groups for molecular electronics: structure and conductance of Au–S–Au and Au–NH₂–Au junctions. *J. Phys. Condens. Matter* **2008**, *20*, 374101.
- [128] Li, R.; Zhang, J.; Hou, S.; Qian, Z.; Shen, Z.; Zhao, X.; Xue, Z. A corrected NEGF+DFT approach for calculating electronic transport through molecular devices: Filling bound states and patching the non-equilibrium integration. *J. Chem. Phys.* **2007**, *336*, 127–135.
- [129] Ren, W.; Reimers, J. R.; Hush, N. S.; Zhu, Y.; Wang, J.; Guo, H. Models for the Structure and Electronic Transmission of Carbon Nanotubes Covalently Linked by a Molecular Bridge via Amide Couplings. *J. Phys. Chem. C* **2007**, *111*, 3700–3704.
- [130] Rocha, C. G.; Torres, L. E. F. F.; Cuniberti, G. ac transport in graphene-based Fabry-Pérot devices. *Phys. Rev. B* **2010**, *81*, 115435.
- [131] Kiran, V.; Cohen, S.; Naaman, R. *J. Chem. Phys.* **2017**, *146*, 092302.
- [132] Kettner, M.; Göhler, B.; Zacharias, H.; Mishra, D.; Kiran, V.; Naaman, R.; Waldeck, D. H.; Şek, S.; Pawłowski, J.; Juhaniwicz, J. Spin Filtering in Electron Transport Through Chiral Oligopeptides. *J. Phys. Chem. C* **2015**, *119*, 14542–14547.
- [133] Larsen, A. H.; Vanin, M.; Mortensen, J. J.; Thygesen, K. S.; Jacobsen, K. W. Localized atomic basis set in the projector augmented wave method. *Phys. Rev. B* **2009**, *80*, 195112.
- [134] Shah, A.; Adhikari, B.; Martić, S.; Munir, A.; Shahzad, S.; Ahmad, K.; Kraatz, H.-B. Electron transfer in peptides. *Chem. Soc. Rev.* **2015**, *44*, 1015–1027.
- [135] Foldy, L. L.; Wouthuysen, S. A. On the Dirac theory of spin 1/2 particles and its non-relativistic limit. *Phys. Rev.* **1950**, *78*, 29.
- [136] McCann, E.; Koshino, M. The electronic properties of bilayer graphene. *Rep. Prog. Phys.* **2013**, *76*, 056503.
- [137] Sewald, N.; Jakubke, H.-D. *Peptides: Chemistry and Biology*; Wiley, 2002.
- [138] Aragonés, A.; et al, *Small* **2016**, *13*, 1602519.
- [139] Mishra, S.; Mondal, A. K.; Pal, S.; Das, T. K.; Smolinsky, E. Z.; Siligardi, G.; Naaman, R. Length-dependent electron spin polarization in oligopeptides and DNA. *J. Phys. Chem. C* **2020**, *124*, 10776–10782.
- [140] Liu, Y.; Xiao, J.; Koo, J.; Yan, B. Chirality-driven topological electronic structure of DNA-like materials. *Nature Materials* **2021**, 1–7.

Abbreviations

–*R* residue 25

α -**HAO** α helix alanine oligopeptide x–xii, 4, 25, 29, 36–41, 49

–CH₃ methyl 25

–COOH carboxyl 25, 31, 35

–NH₂ amino xi, 25, 29, 30, 36, 38

AA amino acid xi, 3, 24, 25, 32, 34

AE all-electron 17, 18

ala alanine xi, 25, 30

ASE atomic simulation environment x, 23, 29, 30

Au gold xi, 29

BO Born–Oppenheimer ix, 6

BZ Brillouin zone 7, 8, 15, 16

CBM conduction band minimum 13

CISS chiral-induced spin selectivity 2, 3, 41, 42

CP-AFM conductive probe atomic force microscopy 3

DFT density functional theory viii, ix, xi, 3–6, 8–12, 14–16, 18, 21–24, 29, 30, 38, 41

DNA deoxyribonucleic acid viii, 2, 3, 35

DOS density of states xii, 36–38, 41

dsDNA double-strand deoxyribonucleic acid 2

DZ double- ζ 16

DZP double- ζ polarized 17, 29, 30

ET electronic transport viii, x, 2–4, 21, 22, 24, 28–31, 35–38, 40–42

FD finite difference 15

GF Green’s function 22, 23

- GGA** generalized gradient approximation 13, 14, 29
GPAW grid-based projector augmented wave method code 3, 16–18, 23, 29, 30, 38, 41
- HEG** homogeneous electron gas 13, 14
HF Hartree-Fock 13
HK Hohenberg–Kohn ix, 8, 9, 12
HOMO highest occupied molecular orbital xi, xii, 11, 17, 30, 36–39, 41
- IBZ** irreducible Brillouin zone 8, 29
- KS** Kohn–Sham ix, xi, xii, 3, 9–16, 18, 29, 36, 38, 40
- LCAO** linear combination of atomic orbitals ix, x, xii, xiii, 3, 15–18, 20, 23, 24, 29–31, 38, 49, 50
LDA local density approximation 13, 14
LSDA local spin-density approximation 14
LUMO lowest unoccupied molecular orbital xi, xii, 17, 30, 36–39, 41
- mc-AFM** magnetic conductive atomic force microscopy 3, 36
- NEGF** non-equilibrium Green’s function viii–x, 4, 21–24, 30, 41
- PAW** projector augmented wave ix, 3, 17, 18, 30
PBC periodic boundary conditions 29, 30
PBE Perdew–Burke–Ernzerhof xc functional 14, 29, 30
PBEsol Perdew–Burke–Ernzerhof xc functional for solids 14
PDOS projected density of states xii, 39
PL principal layer xi, xii, 23, 24, 29, 38, 49, 50
PS pseudo 17, 18
PW plane wave ix, 15, 16
- RAM** random access memory 1
- SDCP** spin-dependent charge polarization 3
SDE spin-dependent electrochemistry 3
SIESTA Spanish initiative for electronic simulations with thousands of atoms code 17
SK Slater–Koster ix–xi, xiii, 18, 19, 28, 31, 41, 43, 45, 47
SO spin orbit viii, xiii, 2, 3, 20, 27, 28, 32, 33, 35, 38, 41, 43
SOC spin-orbit coupling viii, ix, 2, 3, 20, 37
SZ single- ζ 16
SZP single- ζ polarized 17, 30
- TB** tight binding viii–x, 3, 4, 18, 20, 27, 28, 35, 41

TDDFT time-dependent density functional theory 24

TZ triple- ζ 16

VB valence band maximum 13

xc exchange and correlation 3, 9, 11–14, 24, 29, 30